AGU PUBLICATIONS

JGR

Journal of Geophysical Research: Atmospheres

RESEARCH ARTICLE
10.1002/2017JD026677

Key Points:
- OSSEs are conducted to evaluate the value of shortwave and IR spectra for characterizing size-dependent dust loading and sources
- Shortwave or infrared spectra alone lack information for the entire size range of dust aerosols
- Combining shortwave and infrared spectra yields complementary constraints for size-dependent dust loading and emissions

Correspondence to:
X. Xu and J. Wang,
xiaoguang-xu@uiowa.edu;
jun-wang-1@uiowa.edu

Citation:
Xu, X., J. Wang, Y. Wang, D. K. Henze, L. Zhang, G. A. Grell, S. A. McKeen, and B. A. Wielicki (2017), Sense size-dependent dust loading and emission from space using reflected solar and infrared spectral measurements: An observation system simulation experiment, *J. Geophys. Res. Atmos.*, *122*, 8233–8254, doi:10.1002/2017JD026677.

Received 18 FEB 2017
Accepted 14 JUL 2017
Accepted article online 24 JUL 2017
Published online 10 AUG 2017

Sense size-dependent dust loading and emission from space using reflected solar and infrared spectral measurements: An observation system simulation experiment

Xiaoguang Xu[1], Jun Wang[1], Yi Wang[1], Daven K. Henze[2], Li Zhang[3,4], Georg A. Grell[4], Stuart A. McKeen[4], and Bruce A. Wielicki[5]

[1]Department of Chemical and Biochemical Engineering, Center for Global and Regional Environmental Studies, and Informatics Initiative, University of Iowa, Iowa City, Iowa, USA, [2]Department of Mechanical Engineering, University of Colorado, Boulder, Colorado, USA, [3]Cooperative Institute for Research in Environmental Sciences, University of Colorado Boulder, Boulder, Colorado, USA, [4]Earth System Research Laboratory, NOAA, Boulder, Colorado, USA, [5]NASA Langley Research Center, Hampton, Virginia, USA

Abstract The Climate Absolute Radiance and Refractivity Observatory (CLARREO) satellite mission observes hyperspectral Earth reflected solar (RS) and emitted infrared radiance (IR). Such measurements span an additional dimension on spectrally dependent scattering and absorption of dust, the critical signals for particle size. Through a suite of observation system simulation experiments (OSSEs), this study assesses the capability of CLARREO's measurements for recovering size-dependent dust emissions in GEOS-Chem chemistry transport model (CTM). To this end, another CTM (Flow-following finite-volume Icosahedral Model-Chem, or FIM-Chem) is used for the nature run to simulate CLARREO spectral radiances. The spectral signals are then used for analyzing the sensitivities and error characteristics of dust optical depth (DOD) under three observations scenarios (IR only, RS only, and combined IR and RS) using an optimal estimation technique. Next, these synthetic data are assimilated into GEOS-Chem adjoint model to constrain dust emissions of four particle sizes with radii from 0.1 μm to 6.0 μm. The OSSEs results indicate (1) the IR spectra are most sensitive to dust of the third size bin (1.8–3.0 μm) and least sensitive to the smallest bin (0.1–1.0 μm); (2) the RS spectra are most sensitive to dust of the smallest size bin and the sensitivity decreases as dust size increases; (3) combining IR and RS spectra can fully characterize DOD across all sizes, providing the best constraints for size-resolved dust emissions; and (4) CLARREO data fail to constrain the spatial distribution of dust sources due to its narrow swath and joint observations from CLARREO-calibrated sensors with wide swath are desirable.

Plain Language Summary Wind-blown dust particles have a wide range of sizes. This study examines the potential of using measurements in the solar and infrared spectrum from space to characterize and derive the loading and emission of these dust particles in different sizes. The study is important because the climate effect of dust is very uncertain. The study shows that the future satellite missions that measure the solar and infrared spectrum at the same time with high spectral resolution can be used to quantify dust emissions in different sizes and thereby helping to reduce uncertainties in climate predictions.

1. Introduction

Global production and distribution of atmospheric dust varies significantly on daily to intraannual scales owing to the heterogeneity of dust sources and the strong dependence of dust emission on meteorology and climate [e.g., *Knippertz and Todd*, 2012; *Luo et al*., 2004; *Mahowald et al*., 2003; *Guan et al*., 2016]. As a result, prediction of dust distributions and dust radiative impacts in current climate models remains highly uncertain [*Boucher et al*., 2013; *Huneeus et al*., 2011]. Through observation system simulation experiments (OSSEs), this study aims to identify the spectral fingerprint of mineral dust in spaceborne measurements of reflected solar (RS) spectrum and Earth-emitted infrared radiances (IR) and evaluate the capability of these measurements for constraining size-dependent dust loadings and sources.

The upwelling RS and IR radiation at the top of the atmosphere (TOA) regulates the energy budget within the Earth system. Since dust particles have a wide range of sizes from submicron to tens of microns in diameter [*Maring et al*., 2003; *Reid et al*., 2008; *Mahowald et al*., 2014], changes of dust in the Earth system will manifest

Table 1. Existing and Future RS[a] and IR Hyperspectral Satellite Sensors[b]

Type	Satellite Sensor	Spatial Resolution at Nadir (km)	Swath Width (km)	Spectral Range	Spectral Resolution	Radiometric Uncertainty	Available for
RS	GOME	40 × 320	960	240–790 nm	0.2–0.4 nm	2%–5%	1996–2011
	GOME-2	40 × 80 (Metop-A)	1920960	240–790 nm	0.2–0.4 nm	2%–5%	2006 to present
		40 × 40 (Metop-B)					2012 to present
	SCIAMACHY	32 × 215	1000	240–2380 nm	0.24–1.48 nm	2%–4%	2002–2012
	TRUTHS	0.04 × 0.04	40	320–2450 nm	5–10 nm	0.3%	Undetermined
	HyspIRI	0.03 × 0.03	145	380–2500 nm	10 nm	< 5%	Undetermined
	CLARREO and CPF	0.5 × 0.5	100	320–2300 nm	8 nm	0.3%	2020 (CPF)
IR	AIRS	13.5 × 13.5	800	645–2700 cm^{-1}	0.5–2.0 cm^{-1}	0.5 K	2002 to present
	IASI	12 × 12	2000	645–2760 cm^{-1}	0.25 cm^{-1}	0.5 K	2006 to present
	CrIS	13 × 13	2200	645–2700 cm^{-1}	0.6 cm^{-1}	0.2–0.3 K	2011 to present
	CLARREO	25 × 25	25	200–2000 cm^{-1}	0.5 cm^{-1}	0.065 K	Undetermined

[a]Listed are RS spectrometers covering at least the full range of visible spectrum.
[b]Sensor acronyms and references: AIRS, Atmospheric Infrared Sounder [*Hagan and Minnett*, 2003]; CLARREO, Climate Absolute Radiance and Refractivity Observatory [*Wielicki et al*., 2013]; CPF, CLARREO pathfinder mission [*Wielicki et al*., 2016]; CrIS: Cross-Track Infrared Sounder [*Han et al*., 2013]; GOME/GOME-2, Global Ozone Monitoring Experiment (-2) [*Burrows et al*., 1999]; HyspIRI, Hyperspectral InfraRed imager [*Lee et al*., 2015]; IASI, Infrared Atmospheric Sounding Interferometer [*Hilton et al*., 2012];SCIAMACHY, SCanning Imaging Absorption spectroMeter for Atmospheric CHartographY [*Bovensmann et al*., 1999]; and TRUTHS, Traceable Radiometry Underpinning Terrestrial- and Helio-Studies [*Fox et al*., 2003].

in the form of changes of radiation fields in both the RS and IR spectrum through particle scattering and absorption. With this principle, we have used satellite-measured radiances primarily in the RS spectrum to constrain dust emission estimates over the Taklimakan and Gobi deserts of China [*Wang et al*., 2012; *Xu et al*., 2013]. Here we conduct an exploratory study that uses spectrally resolved measurements of radiation in both the RS and thermal IR spectra to constrain the size-dependent dust emissions. While the size-dependent spectral signature of dust particles in IR has been shown in the past studies [cf. *Sokolik*, 2002; *Feldman et al*., 2011; *Xu and Wang*, 2015], such signature also depends on dust optical depth and vertical distribution [*Pierangelo et al*., 2004, 2005; *Vandenbussche et al*., 2013; *Klüser et al*., 2015]. Therefore, a combined use of spectral measurements in both RS and IR may reveal much more information about dust particle size and loading than either alone. However, analysis of how such information from multiple spectra translates into constraints on dust aerosol loading and size-resolved dust emissions has yet to be quantitatively addressed.

Spaceborne sensors have measured upwelling RS and IR spectra at the TOA since a decade ago, and future hyperspectral sensors are expected to provide observations with enhanced accuracy from both geostationary and low-Earth orbiters, such as those listed in Table 1. Existing hyperspectral IR measurement systems include the Atmospheric Infrared Sounder (AIRS), Infrared Atmospheric Sounding Interferometer (IASI), and Cross-track Infrared Sounder (CrIS), which are mainly used to retrieve the profile and structure of air temperature, water vapor, clouds, and trace gases [cf. *Chahine et al*., 2006; *Hilton et al*., 2012; *Han et al*., 2013]. Hyperspectral shortwave measurements available from the SCanning Imaging Absorption spectroMeter for Atmospheric CHartographY (SCIAMACHY) [*Bovensmann et al*., 1999] and Global ozone monitoring experiment (GOME)-1/2 [*Munro et al*., 2016] instruments have been used to determine aerosol properties and the concentration of various atmospheric trace gases. Future climate-oriented satellite observation systems, including Climate Absolute Radiance and Refractivity Observatory (CLARREO) [*Wielicki et al*., 2013] and Traceable Radiometry Underpinning Terrestrial- and Helio- Studies (TRUTHS) [*Fox et al*., 2003, 2011], are being designed to measure Earth-reflected radiances with unprecedented absolute radiometric accuracy. In particular, CLARREO will provide the first simultaneous RS and IR spectral observations covering nearly the entire spectral range. With its accuracy of a factor of 5–10 times better than any current operational space spectrometers, CLARREO will be able to establish benchmark measurements for the detection of the decadal changes in climate forcing and feedbacks through fingerprinting analysis for clouds and water vapor [*Wielicki et al*., 2013; *Jin and Sun*, 2016].

Here we perform OSSEs to evaluate the information content of CLARREO. An OSSE is a technique that can objectively assess the potential added value of future instruments [*Arnold and Dey*, 1986]. It has been extensively used for studying the impact of future satellite observations for weather forecast [*Arnold and Dey*, 1986; *Masutani et al*., 2010], and recently for climate monitoring [*Feldman et al*., 2011, 2015] and for aerosol and air

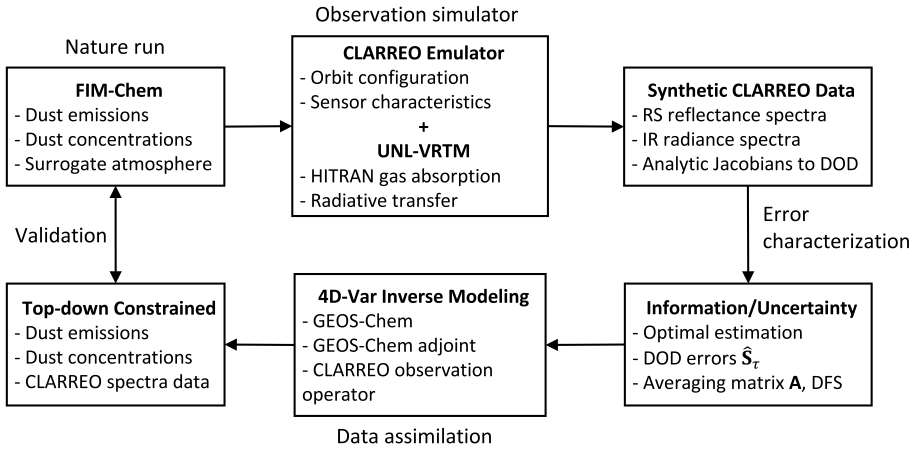

Figure 1. Flowchart of OSSE designed in this study.

quality modeling [*Timmermans et al*., 2009, 2015; *Edwards et al*., 2009; *Meland et al*., 2013]. A standard OSSE has four steps. First, a state-of-the-art atmospheric model is used to generate the reference atmospheric states for the entire OSSE period. This is often called the nature run. Second, observations for the future observing system (CLARREO, in our case) are represented by synthetic observations generated by sampling the nature run according to characteristics of the instrument. Third, these synthetic observations, along with realistically characterized errors and calculated sensitivities, are then assimilated into a different numerical model (referred to as the assimilation model) to generate posterior model parameters. Lastly, the synthetic observations are evaluated by assessing how well the posterior model parameters reproduce the parameters used in the nature run.

In this study, a suite of OSSEs are performed to identify the spectral fingerprints of mineral dust in CLARREO measurements of RS and IR spectra and to objectively evaluate the information content of these measurements for recovering the loading and source of dust aerosols of various sizes. Our hypothesis is that the changes in reflectance/radiance spectra can be ascribed to changes in the size-resolved dust loading and emissions. We emphasize the advantage of the combined use of *both* the RS and IR spectra, as to be measured by CLARREO. Specifically, our OSSE framework integrates global chemistry models, radiative transfer calculations, and a satellite emulator (section 2) to complete the following steps: (i) generate the synthetic CLARREO hyperspectral RS reflectance and IR radiance (section 3.1), (ii) conduct a sensitivity study to identify the dust spectral signature in the CLARREO measurements (section 3.2), and (iii) perform OSSEs to assess the ability of using these spectral signatures to diagnose the size-resolved emission changes of mineral dust (section 3.3).

2. Methodology

2.1. The OSSE Overview

As illustrated in Figure 1, the OSSE framework consists of the following four elements. (1) A chemistry transport model (CTM), in our case the Flow-following finite-volume Icosahedral Model (FIM)-Chem, that performs a nature run to generate a pseudoatmosphere; (2) an observation operator that comprises of an aerosol remote sensing test bed (Unified Linearized Vector Radiative Transfer Model, UNL-VRTM) and a satellite emulator that defines the observing characteristics of CLARREO instruments. The observation operator has capabilities to generate synthetic CLARREO observations from the nature run sampled through the satellite emulator, identify the fingerprint characteristics for dust aerosols, and assess the observational uncertainties for the size-resolved dust optical depths; (3) A CTM with the adjoint-based data assimilation capability (GEOS-Chem adjoint model) to constrain dust emission estimates from the synthetic data; and (4) finally, comparisons of dust emissions between a posteriori and nature run are performed to assess the value of CLARREO measurements for recovering dust emissions. These OSSE components are described in detail in the following subsections.

In our OSSE framework, we use FIM-Chem for the nature run and GEOS-Chem for assimilating the synthetic data. These two models use different meteorological fields affecting the dust aerosols, such as wind speed, soil moisture, and precipitation. The dust aerosol schemes of the two models are also different in the applied soil particle size distribution and preferential source function. Application of two distinct models avoids performing an "identical-twin" OSSE wherein the same model is used for both nature run and data assimilation; in such an OSSE, model errors due to physical parameterization and numerical implementation are neglected and thus can lead to overly optimistic assessment of the impact of synthetic observations [*Arnold and Dey*, 1986; *Masutani et al*., 2010].

It should be noted that satellite level observations of radiance are not directly assimilated in our work. Rather, we assimilate columnar optical depths of sized dust particles. As shown in section 2.6, the assimilation of dust optical depths is indeed equivalent to the assimilation of synthetic radiances when the observational uncertainties are carefully characterized by the synthetic CLARREO observations and because the dust optical properties used in both the nature run and the assimilation run are the same. Our OSSEs consider three scenarios of CLARREO measurements—RS spectra only, IR spectra only, and combined RS and IR spectra (hereafter IR only, RS only, and IR + RS, respectively)—to differentiate the ability of recovering the dust emissions from each observation scenario.

2.2. FIM-Chem Model

FIM-Chem model is used to generate the nature run. FIM is a global Flow-following finite-volume Icosahedral Model (http://fim.noaa.gov/) [*Bleck et al*., 2015] developed in the Global Systems Division of NOAA Earth System Research Laboratory. By integrating FIM and GOCART aerosol chemistry scheme [*Chin et al*., 2000, 2002], FIM-Chem simulates and forecasts aerosol and gas-phase species at various spatial resolutions and with different levels of complexity [*Grell et al*., 2013; *Zhang et al*., 2016b]. The predicted aerosol components include sulfate, dust, sea salt, black carbon, and organic carbon. This study performs FIM-Chem global simulations on 240 km ×240 km icosahedral grids and 64 vertical layers. Its vertical coordinate consists of quasi-Lagrangian isentropic layers in the free atmosphere and terrain-following (sigma coordinate) layers near the ground [*Bleck et al*., 2015].

FIM-Chem uses the AFWA (Air Force Weather Agency) dust emission scheme that was implemented in Weather Research and Forecasting (WRF)-Chem model [*Jones et al*., 2012; *Su and Fung*, 2015], which calculates bulk vertical dust fluxes following the scheme developed by *Marticorena and Bergametti* [1995] (hereafter, the MB scheme) and using the soil particle size distribution developed by *Kok* [2011]. The MB scheme has been widely used in a number of global chemistry transport models, including GEOS-Chem [*Fairlie et al*., 2007], WRF-Chem [*Su and Fung*, 2015], and the dust entrainment and deposition (DEAD) model [*Zender et al*., 2003]. Dust is emitted from bare soil when wind friction velocity exceeds a threshold. The MB scheme determines the threshold friction velocity for dust saltation following *Iversen and White* [1982], simulates the saltation flux over bare soil following *Kawamura* [1951], and uses the sandblasting factor estimated by *Gillette* [1978]. Dust production depends on the magnitude of wind speed, the bareness of the surface, and the moisture and mineralogy of the parent soil. Dust particles in FIM-Chem are separated into five size bins with radii ranging 0.1–1.0 μm, 1.0–1.8 μm, 1.8–3.0 μm, 3.0–6.0 μm, and 6.0–10.0 μm. Each bin is treated as an independent tracer in FIM-Chem. The dust simulation of FIM-Chem has been evaluated against aerosol optical depth observations from the Aerosol Robotic Network (AERONET) [*Grell et al*., 2013; *Zhang et al*., 2016a].

2.3. GEOS-Chem Adjoint Model

The GEOS-Chem adjoint model serves as assimilation model in the OSSE framework. As a global CTM driven by meteorological reanalysis from the Goddard Earth Observing System (GEOS) of NASA's Global Monitoring and Assimilation Office, it includes detailed gas-phase tropospheric chemistry as originally described by *Bey et al*. [2001]. The aerosol simulation in GEOS-Chem includes representations of major aerosol species: sulfate-nitrate-ammonium aerosols [*Park et al*., 2004], black and organic carbon in both hydrophilic and hydrophobic modes [*Park et al*., 2003], mineral dust [*Fairlie et al*., 2007], and sea salts [*Alexander et al*., 2005; *Jaeglé et al*., 2011]. GEOS-Chem couples aerosol and gas-phase chemistry through the effect of aerosol extinction on photolysis rates [*Martin et al*., 2003], aerosol-gas partitioning [*Park et al*., 2004], heterogeneous chemistry [*Jacob*, 2000], and uptake of acidic gases by sea salt and dust [*Evans and Jacob*, 2005]. In this study, we run

full chemistry simulations of GEOS-Chem v8–02-01 with GEOS-5 meteorology over 2° × 2.5° grid cells on 47 vertical layers.

The dust module in GEOS-Chem, originally implemented by *Fairlie et al*. [2007], integrates a dust entrainment and deposition (DEAD) model [*Zender et al*., 2003] and a topographical source function [*Ginoux et al*., 2001]. Similar to the AFWA scheme, DEAD model also employs the MD scheme for calculating saltation flux. Dust particles in GEOS-Chem are characterized in four size bins with radii ranging 0.1–1.0 μm, 1.0–1.8 μm, 1.8–3.0 μm, and 3.0–6.0 μm [*Zhang et al*., 2013], which are the same as the first four size bins in FIM-Chem. Hereafter, we use DST1, DST2, DST3, and DST4 to represent these four dust size bins and focus on the inversion of dust emissions in these four size bins. While freshly emitted dust aerosols contain a substantial mass of particles with radii larger than 6 μm, as observed during the Fennec field campaign in the Sahara Desert [*Ryder et al*., 2013], those large-size particles, however, are quickly removed by gravitational settling within a day and have a limited transport distance [*Chin et al*., 2002; *Maring et al*., 2003; *Mahowald et al*., 2014]. As a result, the overall mass loading of dust larger than 6 μm in radius only accounts for about 2% of the dust mass loading across the entire size [*Tegen and Lacis*, 1996]. The most recent results from *Kok et al*. [2017] revealed a 3%–15% global contribution from dust greater than 5 μm in radius. Furthermore, dust size bins are independent of each other. Therefore, we neglect the dust emission for the fifth size bin in FIM-Chem and choose not to assimilate its corresponding DOD.

The adjoint of the GEOS-Chem model was developed specifically for inverse modeling of aerosol and gas emissions [*Henze et al*., 2007]. It uses adjoint-based four-dimensional variational (4D-Var) approach to constrain aerosol emissions. As such, the tool has been extensively used in inverse modeling studies that include evaluation of aerosol and aerosol precursor emissions [*Henze et al*., 2009; *Wang et al*., 2012; *Xu et al*., 2013; *Qu et al*., 2016; *Y. Wang et al*., 2016]. The adjoint code was developed using a combination of manually derived adjoint code and generic automatic differentiation tools. Gradients from the adjoint are used with the L-BFGS-B quasi-Newton gradient optimization routine [*Zhu et al*., 1994; *Byrd et al*., 1994] for inverse modeling. The numerical accuracy of these gradients are extensively and routinely verified through comparison to sensitivities from finite difference simulations [*Henze et al*., 2007].

2.4. Radiative Transfer Calculation of Synthetic CLARREO Data

The synthetic data include observations for two hyperspectral instruments to be equipped on the CLARREO platform, i.e., an IR spectrometer and a RS spectrometer [*Wielicki et al*., 2013]. We develop a satellite emulator that simulates the CLARREO-observing strategy in the aspects of orbital track, scanning geometry, field of views, spectral configuration of the carried instruments, solar beam geometry, and observation error characteristics. The CLARREO satellite was designed to fly the 90 degree-inclined precessionary polar orbit at an altitude of 609 km and revisit a certain location every 61 days. Its orbit repeats exactly each year to avoid diurnal/seasonal cycle aliasing. The IR spectrometer will measure spectrally resolved infrared radiances (from 200 to 2000 cm^{-1} with 0.5 cm^{-1} unapodized spectral resolution) emitted from Earth to space with an accuracy of 0.06 K for the equivalent brightness temperature (BT). This instrument is designed to scan a 25 km pixel at nadir in a 200 km distance along the ground track. The RS spectrometer measures spectrally resolved reflectance of solar radiation in ultraviolet (UV), visible, and near-infrared (NIR) spectrum (0.32–2.3 μm) with an accuracy of 0.3% relative to the mean spectral reflectance of the Earth of about 0.3. While the swath of the RS spectrometer is 100 km wide, consisting of 200 0.5 km cross-track pixels, reflectance spectra of native spectral resolution (full width at half maximum = 8 nm) will only be reported at an aggregated 10 km spatial resolution. Given these instrument spatial resolutions, one FIM-Chem model grid tends to contain a single IR nadir observation but about two hundred 10 km pixels of the RS observations. Clearly, the nature run is unable to resolve the spatial resolution of RS measurements; data thinning is required. Therefore, RS observations are spatially averaged over the model grid, thereby pairing each RS observation with an IR observation.

The synthetic spectral radiances are calculated by UNL-VRTM, which was specifically developed as a numerical test bed for the analysis and inversion of remote sensing observations [*Wang et al*., 2014]. UNL-VRTM consists of various modules for forward calculation of synthetic observations and a module for optimal inversion. The forward modeling includes a linearized vector radiative transfer model (VLIDORT) [*Spurr*, 2006], linearized Mie and T-Matrix codes [*Spurr et al*., 2012], and modules calculating Rayleigh scattering and gas absorption, plus a surface model computing various bidirectional

reflectance distribution functions [*Spurr*, 2004]. The aerosol-related modules—Mie, T-matrix, and VLIDORT—are analytically linearized and fully coupled. Thus, UNL-VRTM not only simulates spectral radiances but also computes the Jacobians of radiances with respect to aerosol optical and microphysical parameters. This inversion-oriented test bed supplies these Jacobians together with observation error characterizations and a priori constraints to a statistical optimization procedure to perform information content and error analysis [*Xu and Wang*, 2015]. UNL-VRTM has been used to retrieve aerosol microphysical parameters from AERONET photopolarimetric measurements [*Xu et al*., 2015], to simulate Visible Infrared Imaging Radiometer Suite (VIIRS) day-and-night band [*J. Wang et al*., 2016], to examine the aerosol profile information contained in the spectral radiance over the oxygen A and B bands [*Ding et al*., 2016; *Xu et al*., 2017], and to determine the surface reflectance spectra from Geo-TASO measurements [*Hou et al*., 2016, 2017].

Synthetic CLARREO data are limited to over-ocean pixels in order to avoid the complexity of spectral reflectance and emissivity of land surfaces. The influences of cloudiness and sunglint on the data availability are also neglected. In the RS spectrum, we assume a Lambertian ocean surface with spectral reflectance obtained from the Advanced Spaceborne Thermal Emission and Reflection Radiometer library [*Baldridge et al*., 2009]. The emissivity of the ocean surface is assumed to be 0.95 across the IR spectra. Profiles of aerosol and water vapor concentration and relevant meteorological fields from the nature run are utilized by UNL-VRTM for generating synthetic data for each CLARREO scan. Specifically, we take air temperature, pressure, liquid water content, specific humidity, and dust mass concentrations of the size bins 1–4. Also considered in the UNL-VRTM is absorption by various trace gases including carbon dioxide (CO_2), ozone (O_3), nitrous oxide (N_2O), nitrogen dioxide (NO_2), methane (CH_4), and oxygen (O_2), the profiles of which are taken from a tropical standard atmosphere [*McClatchey et al*., 1972].

In the calculation of dust optical properties, we assume dust are spherical particles following a lognormal size distribution function within each size bin, and the smallest bin is further represented by four subsize bins [*Chin et al*., 2002]. Dust median radius was defined by *Chin et al*. [2002]. Geometric standard deviation of dust radius was updated by *Drury et al*. [2010]. The dust nonsphericity is not considered because shapes of dust particles are not unique and difficult to characterize [*Wang et al*., 2003]. We use the spectral dependent dust refractive index measured by *Patterson et al*. [1977] and updated by *Wang et al*. [2003] for the RS spectra and compiled by *Di Biagio et al*. [2014] for the IR spectra, both assumed to be independent of dust particle size. Figures 2a and 2b presents the spectral refractive index, as well as calculated mass extinction efficiency. It should be noted that refractive index depends on mineralogy and chemical composition of dust particles and is thus subjective to substantial regional variability, especially in the infrared [*Di Biagio et al*., 2014; *Mahowald et al*., 2014; *Scanza et al*., 2015; *Perlwitz et al*., 2015]. Given that both chemistry transport models are not able to simulate dust aerosols at the mineralogical level, we use the average value of refractive indices observed for dust from different locations [*Di Biagio et al*., 2014]. It is worth mentioning that *Di Biagio et al*. [2017] recently reported a new LW dust refractive index database with more samplings from different regions, which are valuable to address regionally dependent dust properties.

2.5. Calculation of Sensitivity and Information Content

We briefly present how to assess the sensitivity and information content of CLARREO measurements to the dust aerosol loading (i.e., dust optical depth or DOD) of different sizes. Conceptually, the radiative transfer modeling process can be expressed by

$$\boldsymbol{\rho} = F(\boldsymbol{\tau}) + \boldsymbol{\epsilon} \tag{1}$$

where $\boldsymbol{\rho}$ is an observation vector comprising spectral RS reflectance and IR radiances to be measured by CLARREO instruments, $\boldsymbol{\tau}$ is a state vector of DOD over four dust size classes, $F(\ )$ is the forward operator (i.e., UNL-VRTM) that explicitly associates any elements in $\boldsymbol{\tau}$ to any elements in $\boldsymbol{\rho}$, and $\boldsymbol{\epsilon}$ is an experimental error term. Assuming $\boldsymbol{\tau}$ is linearly related to $\boldsymbol{\rho}$ in their vicinity (represented by $\boldsymbol{\tau}_0$ and $\boldsymbol{\rho}_0$), the forward model can be expressed by

$$\boldsymbol{\rho}_0 = \mathbf{K}\boldsymbol{\tau}_0 + \boldsymbol{\epsilon} \tag{2}$$

where $\mathbf{K}$ is the Jacobian matrix, a matrix of first-order partial derivatives of $F(\boldsymbol{\tau})$ with respect to $\boldsymbol{\tau}$ at $\boldsymbol{\tau} = \boldsymbol{\tau}_0$. $\mathbf{K}$ is analytically calculated in the UNL-VRTM along with the simulation of $F(\boldsymbol{\tau})$. Our sensitivity analysis uses

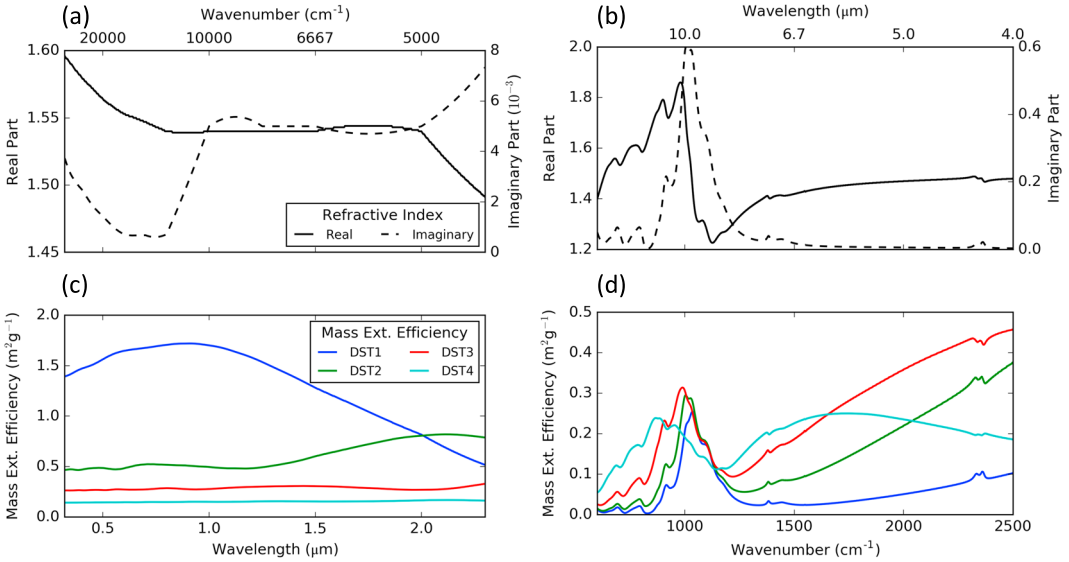

Figure 2. Complex refractive index of mineral dust for (a) RS and (b) IR spectra and (c and d) calculated mass extinction efficiency for each dust bin. Note that spectral range is denoted in wavelength (in μm) for RS spectra and in wave number (in cm^{-1}) for IR spectra throughout the article; double axes are used to provide their conversion.

normalized Jacobian, which is defined as $\tau\frac{\partial\rho}{\partial\tau}$ to represent the change of radiance signal in ρ produced by per magnitude change of τ.

Given the characteristics of the Gaussian-type observation error and a priori error, the information content of $\boldsymbol{\rho}$ for determining $\boldsymbol{\tau}$ can be quantified by the degree of freedom for signals (DFS) that is calculated from an averaging kernel matrix $\mathbf{A}$ based on the Bayesian approach [*Rodgers*, 2000; *Xu and Wang*, 2015]. The matrix $\mathbf{A}$ in a linear inverse problem is calculated by

$$\mathbf{A} = \left(\mathbf{K}^T\mathbf{S}_\rho^{-1}\mathbf{K} + \mathbf{S}_{\tau,\mathrm{a}}^{-1}\right)^{-1}\mathbf{K}^T\mathbf{S}_\rho^{-1} \tag{3}$$

where $\mathbf{S}_\rho$ and $\mathbf{S}_{\tau,\mathrm{a}}$ are the covariance matrices of observation and prior errors, and T indicates the transpose operation. In this study, $\mathbf{A}$ is a 4×4 matrix as the state vector $\boldsymbol{\tau}$ has four elements. DFS is defined as the trace of $\mathbf{A}$

$$\mathrm{DFS} = \sum\nolimits_i \mathrm{DFS}_i = \sum\nolimits_i \mathrm{diag}(\boldsymbol{A})_i. \tag{4}$$

The diagonal element of $\mathbf{A}$ is thus called DFS component (DFS_i), which represents the partial sensitivity of each individual retrieval parameter with respect to its truth. For instance, $\mathrm{DFS}_i = 1$ indicates that the observations are fully capable of characterizing τ_i, while $\mathrm{DFS}_i = 0$ means the observations contain no information for τ_i, where τ_i represents DOD of the size bin i. Correspondingly, the posterior error covariance matrix $\hat{\mathbf{S}}_\tau$ is defined by

$$\hat{\mathbf{S}}_{\boldsymbol{\tau}} = \left(\mathbf{K}^T\mathbf{S}_\rho^{-1}\mathbf{K} + \mathbf{S}_{\tau,\mathrm{a}}^{-1}\right)^{-1}. \tag{5}$$

$\hat{\mathbf{S}}_{\boldsymbol{\tau}}$ represents the statistical uncertainties of the retrieved $\boldsymbol{\tau}$, with retrieval error corresponding to each diagonal element of $\hat{\mathbf{S}}_\tau^{\frac{1}{2}}$.

According to equations (3) and (5), the resulting DFS and retrieval error depend on the specification of prior error and observation error. A realistic uncertainty characterization is thus of critical importance to determine the impact of the observations. Here prior DODs are assumed to have a relative error of 50% plus an absolute error of 0.2, 0.15, 0.1, and 0.05 for the four dust size bins, respectively. This assumption is based on the fact that DOD simulated by GEOS-Chem often has a normalized mean bias of 10%–70% [*Johnson et al*., 2012; *Wang et al*., 2012; *Xu et al*., 2013; *Ridley et al*., 2014, 2016]. The included absolute error of each size bin corresponds to a 50% error for a typical total DOD value of 1.0, which serves as an error cap to ensure a stable matrix inversion. These prior errors of each size bin are assumed uncorrelated, because bin-based dust tracers are treated independently in the modeling process.

Observation errors usually account for forward model errors that stem from uncertainties in model parameters and inaccuracy in representing physics by the model, in addition to the instrumental noise. For example, accuracy in the thermal radiances calculated from the GEOS-Chem observation operator strongly depends on assumptions of surface emissivity, dust microphysical properties, and meteorological fields (such as the air and surface temperatures and water vapor content). Therefore, in addition to the instrumental uncertainties (0.06 K for IR BT and 0.001 for RS reflectance), observation errors include large contributions from GEOS-Chem forward modeling mainly caused by (1) errors in the prescribed dust refractive indices, (2) errors from the surface reflectance, and (3) errors in the assumed ocean surface emissivity. In this study, we assume a one-sigma error of 0.4 K for BT across the IR spectra and 0.03 ± 5% (i.e., an absolute error of 0.03 plus a relative error of 5%) across the RS spectra, both following a Gaussian distribution. The 0.4 K level of BT uncertainty represents a typical accuracy of in situ measurement for calibrating satellite instruments [*Emery et al*., 2001]. It should be noted that we do not consider representativeness errors by assuming homogeneous aerosol properties within each model grid over the ocean, because the nature run model has a similar resolution as the assimilation model. The error covariance matrix (expressed by $\mathbf{S}_\rho$ in the following section) includes off-diagonal elements to account for spectral redundancy and GEOS-Chem forward modeling error correlations. Here we assume error correlations simply decay with sampling distance in the spectral space: correlation coefficients are 0.95 and 0.66 for the closest and second closest adjacent channel pairs, and 0.33 in any other pair-wise channels.

2.6. Adjoint-Based 4D-Var Inversion of Dust Emissions

In GEOS-Chem adjoint, aerosol emissions are constrained by an adjoint-based 4D-Var inverse technique [*Henze et al*., 2007]. Dust emissions are adjusted using a vector of control parameters $\boldsymbol{\sigma}$ that are the logarithm of emission scaling factors in each grid cell, $\sigma(i,j) = \ln[E(i,j)/E_a(i,j)]$, where $E(i,j)$ and $E_a(i,j)$ are updated and prior aerosol emission amounts in grid cell (i,j). The cost function is formulated following the 4D-Var technique comprising a model error term and a penalty term. Our OSSEs are designed to assimilate DODs with uncertainty characterized by synthetic CLARREO data. The cost function is expressed by

$$J(\boldsymbol{\sigma}) = \frac{1}{2}[\boldsymbol{\tau}(\mathbf{c}) - \boldsymbol{\tau}_{\mathbf{obs}}]^T \hat{\mathbf{S}}_{\boldsymbol{\tau}}^{-1}[\boldsymbol{\tau}(\mathbf{c}) - \boldsymbol{\tau}_{\mathbf{obs}}] + \frac{1}{2}(\boldsymbol{\sigma} - \boldsymbol{\sigma}_{\mathbf{a}})^T \mathbf{B}^{-1}(\boldsymbol{\sigma} - \boldsymbol{\sigma}_{\mathbf{a}}), \tag{6}$$

where $\boldsymbol{\tau}_{\mathbf{obs}}$ indicates a vector of available observations in the time and space domain, $\boldsymbol{\tau}(\mathbf{c})$ is an observation operator that maps aerosol concentration vector $\mathbf{c}$ to the observation space, $\hat{\mathbf{S}}_{\boldsymbol{\tau}}$ is the error covariance matrix of $\boldsymbol{\tau}_{\mathbf{obs}}$ characterized by synthetic CLARREO data in equation (5), and $\boldsymbol{\sigma}_{\mathbf{a}}$ is the vector of prior emission scaling factors characterized by an error covariance matrix $\mathbf{B}$. In this study, we assume a relative error of 100% for prior emission estimates following *Xu et al*. [2013]. The optimal estimate of $\boldsymbol{\sigma}$ corresponds to the minimum of the cost function, which balances the objectives of minimizing mismatch between model and observations while ensuring $\boldsymbol{\sigma}$ remains within an appropriate range described by $\mathbf{B}$.

Using $\hat{\mathbf{S}}_\tau$ of equation (5), we can rewrite equation (6) as

$$\begin{aligned} J(\boldsymbol{\sigma}) = {} & \frac{1}{2}[\mathbf{K}\boldsymbol{\tau}(\mathbf{c}) - \mathbf{K}\boldsymbol{\tau}_{\mathrm{obs}}]^T \mathbf{S}_\rho^{-1}[\mathbf{K}\boldsymbol{\tau}(\mathbf{c}) - \mathbf{K}\boldsymbol{\tau}_{\mathrm{obs}}] + \frac{1}{2}[\boldsymbol{\tau}(\mathbf{c}) - \boldsymbol{\tau}_{\mathrm{obs}}]^T \mathbf{S}_{\boldsymbol{\tau},\mathbf{a}}^{-1}[\boldsymbol{\tau}(\mathbf{c}) - \boldsymbol{\tau}_{\mathrm{obs}}] \\ & + \frac{1}{2}(\boldsymbol{\sigma} - \boldsymbol{\sigma}_{\mathbf{a}})^T \mathbf{B}^{-1}(\boldsymbol{\sigma} - \boldsymbol{\sigma}_{\mathrm{a}}). \end{aligned} \tag{7}$$

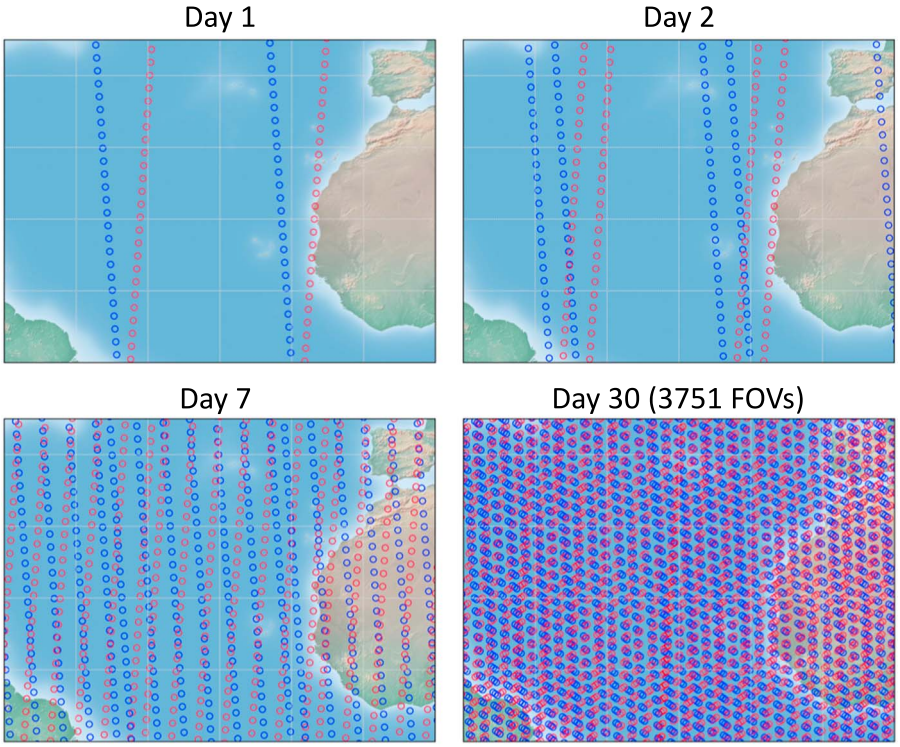

Figure 3. Emulated subtrack footprints of the CLARREO's precessionary orbit for 1, 2, 7, and 30 days of overpass in the selected observation domain (60°W to 0°E, 0°N to 45°N). Each circle indicates one scan by the IR spectrometer. Blue and red colors indicate scans from ascending and descending orbits, respectively.

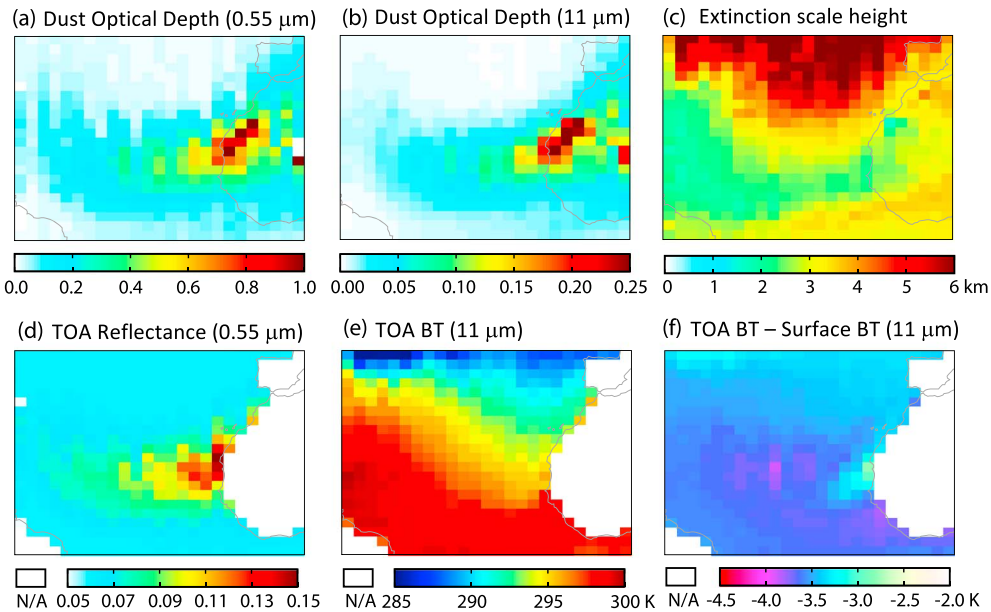

Figure 4. Geographical distribution of DOD at spectral wavelengths of (a) 0.55 μm and (b) 11 μm, (c) scale height of dust extinction at 0.55 μm, (d) synthetic TOA reflectance at 0.55 μm, (e) brightness temperature (BT) at 11 μm, and (f) BT difference of TOA and sea surface. Those quantities are sampled from synthetic data for CLARREO orbits during June 2011. Scale height is defined as the above ground level altitude below which the aerosol extinction accounts for 63% (equal to $1 - e^{-1}$) of the total columnar aerosol extinction (following *Yu et al.* [2010]).

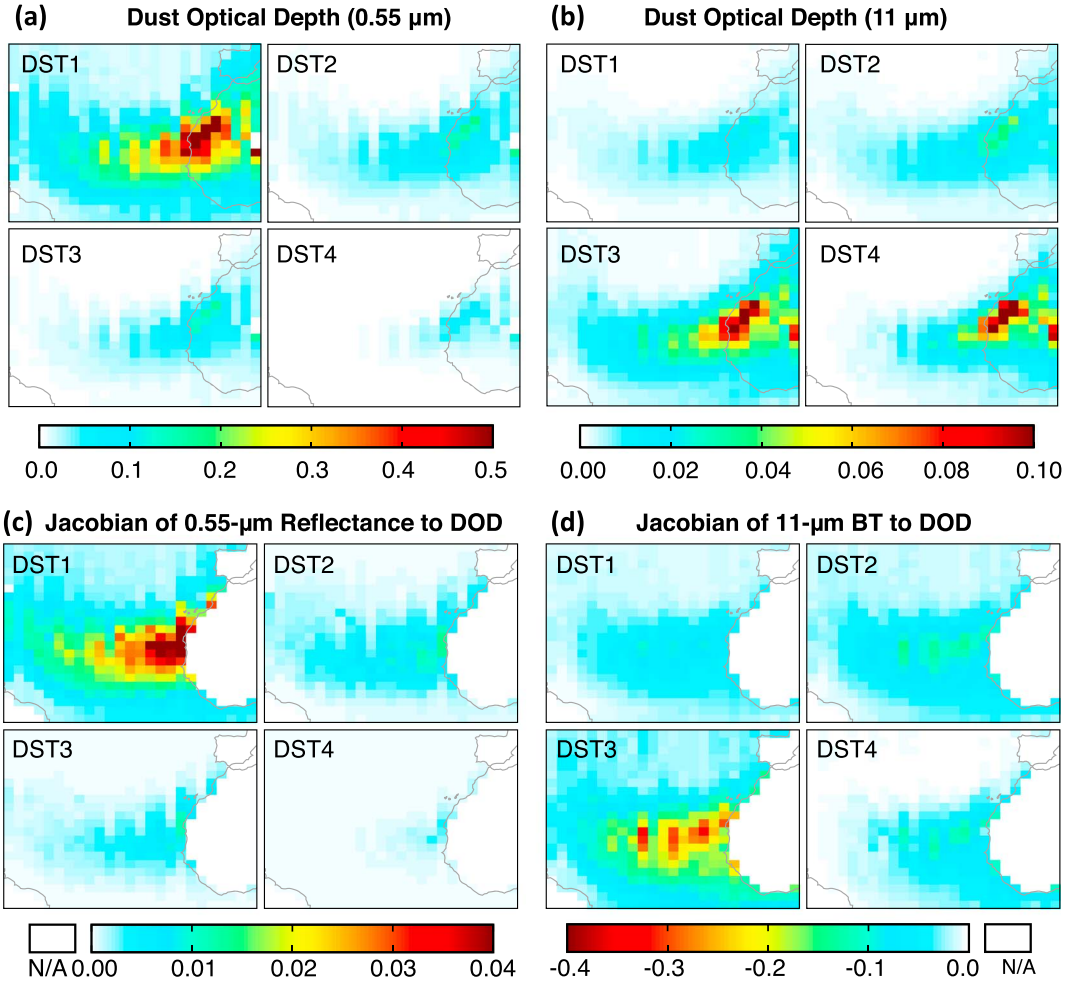

Figure 5. Geophysical distribution of synthetic CLARREO DOD of each size bin at wavelengths of (a) 0.55 μm and (b) 11 μm, (c) Jacobians of 0.55 μm reflectance, and (d) 11 μm BT with respect to DOD of each size bin. Note the change in color bar for each panel.

Because identical aerosol optical properties are used in the radiance calculation for both FIM-Chem nature run and GEOS-Chem run, $\boldsymbol{\rho}(\mathbf{c}) = \mathbf{K}\boldsymbol{\tau}(\mathbf{c})$ and $\boldsymbol{\rho}_{\text{obs}} = \mathbf{K}\boldsymbol{\tau}_{\text{obs}}$. As a result, equation (7) becomes

$$J(\boldsymbol{\sigma}) = \frac{1}{2}[\boldsymbol{\rho}(\mathbf{c}) - \boldsymbol{\rho}_{\text{obs}}]^T \mathbf{S}_{\rho}^{-1}[\boldsymbol{\rho}(\mathbf{c}) - \boldsymbol{\rho}_{\text{obs}}] + \frac{1}{2}(\boldsymbol{\sigma} - \boldsymbol{\sigma}_{\text{a}})^T \mathbf{B}^{-1}(\boldsymbol{\sigma} - \sigma_{\text{a}}) + \frac{1}{2}[\boldsymbol{\tau}(\mathbf{c}) - \boldsymbol{\tau}_{\text{obs}}]^T \mathbf{S}_{\tau,\text{a}}^{-1}[\boldsymbol{\tau}(\mathbf{c}) - \boldsymbol{\tau}_{\text{obs}}]. \quad (8)$$

The first two terms of equation (8) indeed represent 4D-Var assimilation of satellite radiances. The third term acts as prior DOD constraints that confine updated DOD values to a realistic magnitudes defined by $\mathbf{S}_{\tau,\text{a}}$. Therefore, our assimilation of DOD is equivalent to the direct assimilation of synthetic radiances with additional prior DOD constraints.

3. Results

We focus our OSSEs on trans-Atlantic dust aerosols emitted from the Sahara Desert, where the influence from other aerosol sources is relatively small. FIM-Chem performs a nature run for a 1 month period during June 2011 with 1 month spin-up, based on which we generate synthetic CLARREO measurements of IR and RS spectra over the downwind Atlantic regions. As shown in Figure 3, CLARREO overpasses 4 to 5 times each day over the defined domain (60°W to 0°E, 0°N to 45°N), leading to 3751 scans by the IR spectrometer in

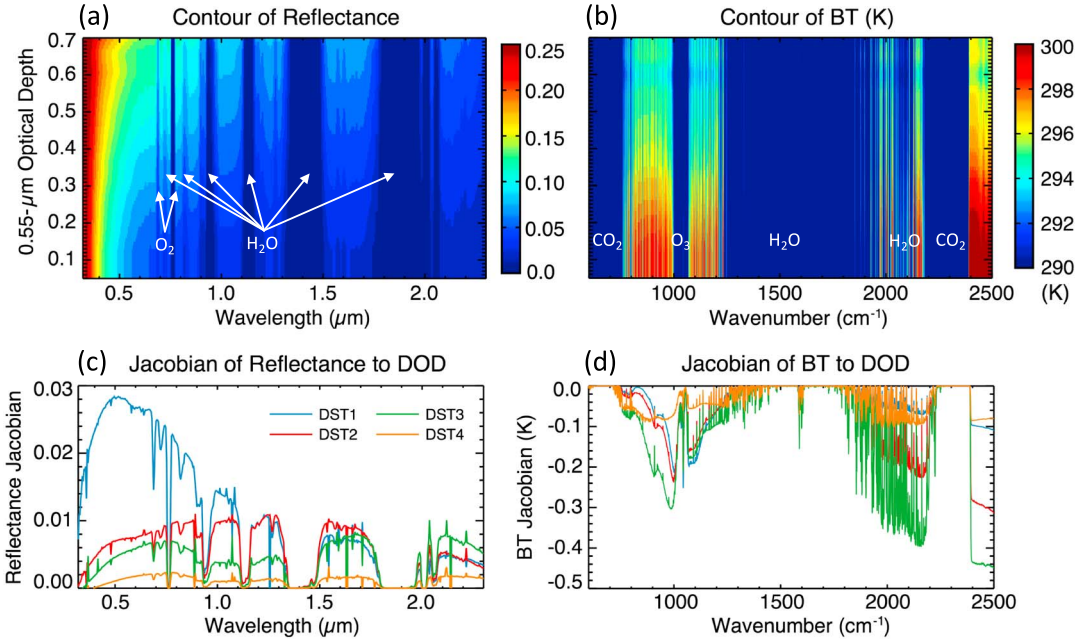

Figure 6. Synthetic CLARREO spectra of (a) RS reflectance and (b) IR BT and (c and d) averaged Jacobians of these spectra with respect to DOD of different sizes. In Figures 6a and 6b, *x* axis indicates spectral domain, and the change of spectra along with 0.55 μm DOD is indicated in *y* axis. Here DOD is binned at 0.05 intervals, and contours are the spectra averaged on DOD bins. Spectral bands with dominated gases absorption from O_2, H_2O, O_3, and CO_2 are also annotated. In Figures 6c and 6d, the spectral Jacobians are averaged for the CLARREO samplings with 0.55 μm DOD larger than 0.05.

1 month. Three scenarios of these measurements (i.e., IR only, RS only, and IR + RS) are considered to assess the capability to determine dust loading and emission from different spectral radiance signals. In this section, we first present the synthetic CLARREO data at 0.55 μm and 11 μm bands with a focus on their geographical distribution (section 3.1), then examine the dust spectral signatures and the information content of CLARREO measurements (section 3.2) to retrieve size-dependent DOD, and lastly investigate the capability of each observation scenario for constraining size-resolved dust emissions (section 3.3).

3.1. Geographical Distribution of Synthetic Data

Figures 4a and 4b show the monthly averages of 0.55 μm and 11 μm total DOD that are simulated by the FIM-Chem nature run and sampled at the CLARREO observing time and location. Corresponding DODs of each size bin are displayed in Figures 5a and 5b. According to these maps, dust plumes are emitted from the Saharan deserts and are transported across the Atlantic Ocean to the eastern coast of Central and Northern America. Dry and wet deposition of dust particles occur during transport, resulting in an obvious gradient with high dust loading near the source regions. The 11 μm DODs are smaller than that of 0.55 μm due to lower extinction coefficients of dust in IR spectrum (Figure 2), especially for the smallest dust size bin that contributes over half portion of the 0.55 μm DOD (Figures 5a and 5b).

The geographical distribution of CLARREO reflectance at 0.55 μm is shown in Figure 4d; the 11 μm BT at TOA and the BT difference between TOA and sea surface are presented in Figures 4e and 4f. Figures 5c and 5d display the spatial distribution of normalized Jacobians of 0.55 μm reflectance and 11 μm BT to DOD of each dust size, which quantify the changes of radiance signals caused by one magnitude change of DOD of a given size bin. Clearly, the presence of dust over the ocean enhances the reflectance at visible band by scattering solar radiation back into space. The strongest signal in visible reflectance arises from the dust aerosol in the first size bin (Figure 5c). In the IR band, while the BT signal is dominated by the latitudinal gradient of ocean temperature (Figure 4d), significant decreases in BT exist over elevated dust plumes (Figures 4f and 4c) due to the thermal contrast between the surface and the above air where the dust particles reside [e.g., *Ackerman*, 1997; *Sokolik*, 2002]. The average magnitude of BT reduction reaches as high as 4 K, 10 times larger than the typical observational BT uncertainty. Comparing each bin, such BT

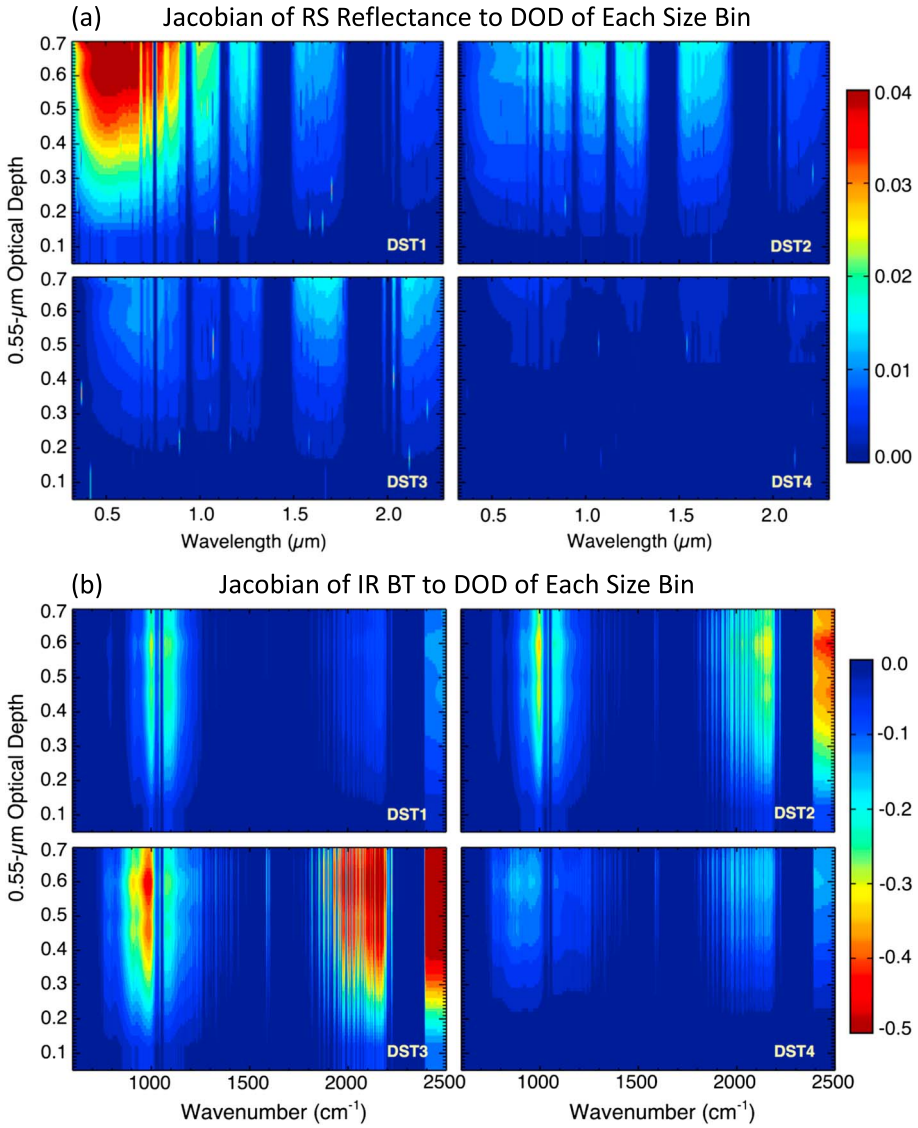

Figure 7. Same as Figures 6a and 6b but for spectrally resolved Jacobians of synthetic (a) CLARREO RS reflectance and (b) IR BT to DOD of each size class.

reduction is mainly produced by larger dust size bins, particularly the third bin (Figure 5d). Therefore, the IR radiance signals, as well as RS reflectance, can manifest the change of dust loading and contain information for determining dust properties of different sizes.

3.2. Spectral Signature of Dust and Information Content Analysis

Since our study uses synthetic CLARREO data over the tropical Atlantic Ocean where surface reflectance is generally low and surface temperature varies smoothly within a difference of 3 K, the RS reflectance and IR radiance depend mainly on the dust loading in addition to gas absorption. To investigate the impact of dust loading on these upwelling spectra, we plot in Figures 6a and 6b the spectra of RS reflectance and IR BT as a function of 0.55 μm DOD. The rapid decrease of reflectance from UV to visible is caused by scattering of light by air molecules, known as Rayleigh scattering. The spectral discontinuity in reflectance and BT results from the strong absorption by trace gases, such as O_2 and H_2O (water vapor) in RS spectra and H_2O, CO_2, and O_3 in IR spectra (Figures 6a and 6b). In these spectral regions of gaseous absorption, air transmittance is close to zero and radiance signal is insensitive to dust. Outside of gaseous absorption bands, RS reflectance increases and IR BT decreases with the increase of DOD.

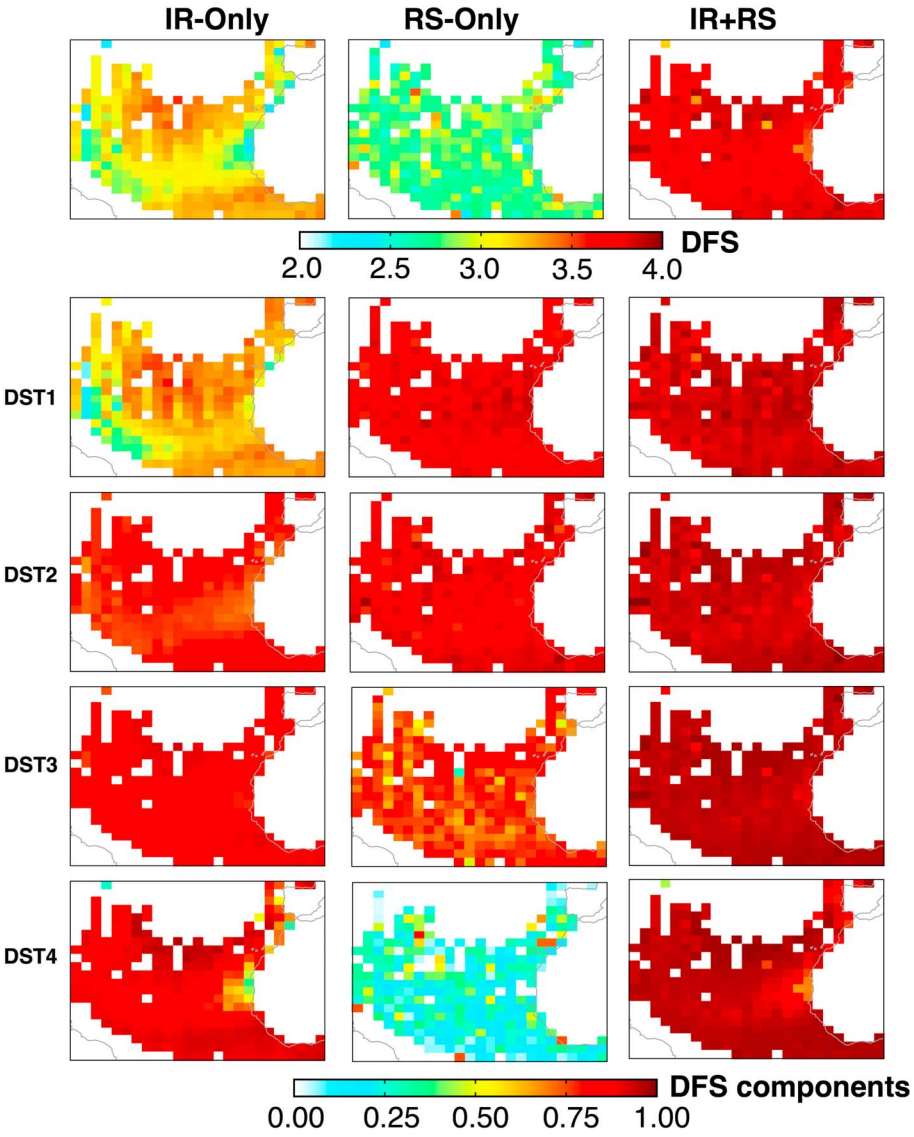

Figure 8. (first row) DFS for retrieving DOD of four size classes and (second to fifth rows) DFS components for each size class. Three columns correspond to CLARREO observation configurations of IR only, RS only, and IR + RS, respectively. Note that DFS in Figure 8 (first row) is the sum of all DFS components in Figure 8 (second to fifth rows), as defined in equation (4).

We compute the spectrally resolved Jacobians to DOD of each size bin calculated by UNL-VRTM to quantify the information content of CLARREO for the size-dependent dust loadings. Figures 6c and 6d show the mean spectral sensitivity (normalized Jacobian) based on synthetic data over the study domain, and Figure 7 shows the change of these spectral Jacobians with the total DOD. Concerning dust loading, sensitivities increase as the DOD increases. It is straightforward that the presence of more dust aerosols in the atmosphere leads to stronger radiative signal in the synthetic data in both the RS and IR spectra. Higher sensitivity occurs in atmospheric window channels with weak gaseous absorption.

As seen from Figures 6c and 7a, the sensitivities in the RS spectra exhibit distinct magnitude and spectral variability among different size bins. For instance, the change of DOD in the first size bin can lead to the strongest perturbation of spectral reflectance in the visible band; yet, such perturbation decreases along with the increase of spectral wavelength. In contrast, sensitivity to DOD of the second bin peaks in the NIR region of 1–2 μm. Compared with that of the first bin, the Jacobian of reflectance to DOD of the second bin is smaller

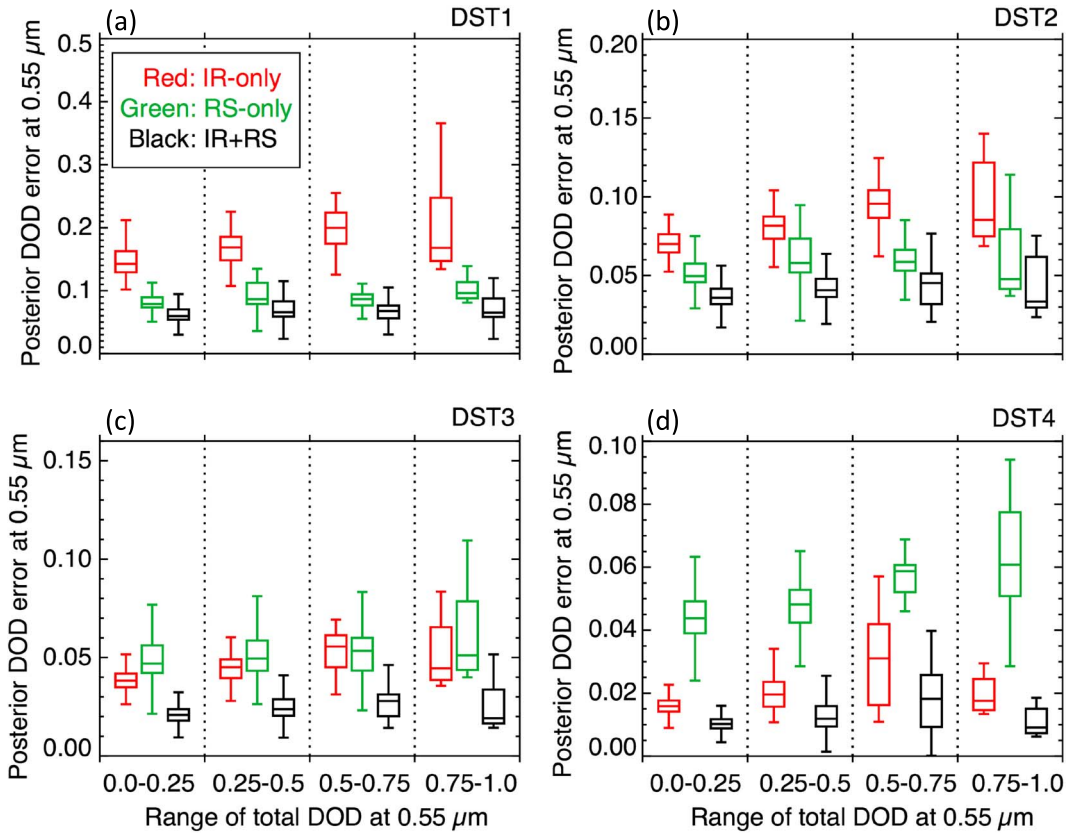

Figure 9. (a–d) Boxplots of DOD retrieval error of each size bin derived from equation (5) for 0.55 μm DOD within 0.0–0.25, 0.25–0.5, 0.5–0.75, and 0.75–1.0, respectively. Three different colors, i.e., red, green, and black, indicate observation configurations of IR only, RS only, and IR + RS, respectively. The bottom and top of the box and the band inside the box indicate the first and third quartiles and the median, respectively. The ends of whiskers represent the lowest and highest data within 1.5 interquartile range of the lower and higher quantiles, respectively [*Frigge et al.*, 1989].

in the UV and visible bands but over 2 times larger in the NIR bands. Sensitivity of reflectance to DST4 is rather small across the RS spectra because such large-size particle is optically less significant comparing to the other three size bins (Figure 2). Similarly, sensitivities of BT in IR spectra show obvious size dependency but with the least magnitude for DST1 and DST4 (Figures 6d and 7b).

DFS is computed to examine the quantitative information on size-dependent DOD contained in synthetic data for three configurations of observed spectra, i.e., IR only, RS only, and combined IR and RS spectra (IR + RS). Figure 8 shows the spatial distribution of overall DFS (first row) as well as the DFS component for DOD of each size bin (second to fifth rows) over the study domain. As expected, IR spectra are most informative to DOD of the third size class and least to DOD of the first size bin (Figure 8, left column). In contrast, the RS spectra can be used to best retrieve the DOD of the first and second size bins (Figure 8, middle column); information decreases as dust size increases. This is because small scattering particles tend to be transparent in the IR spectrum, and large particles are relatively less optically significant in the shortwave spectrum (Figure 2). Combining the complementary information of RS and IR spectra allows the DFS component for DOD of all size classes close to approach unity in each grid cell—information for fully characterizing dust size is nearly 100% (Figure 8, right column).

Along with DFS, the posterior error covariance matrix is also calculated using equation (5). Figure 9 displays boxplots of posterior error versus the synthetic DODs of each size bin. We associate these posterior uncertainties to each DOD value, which are assimilated by the GEOS-Chem adjoint model in our OSSEs. As expected, DOD obtained from RS spectra demonstrates better accuracy than that from IR spectra for DST1 and DST2 but is less accurate for DST3 and DST4. Combined IR and RS measurements deliver lowest DOD uncertainties (black) for all four size bins.

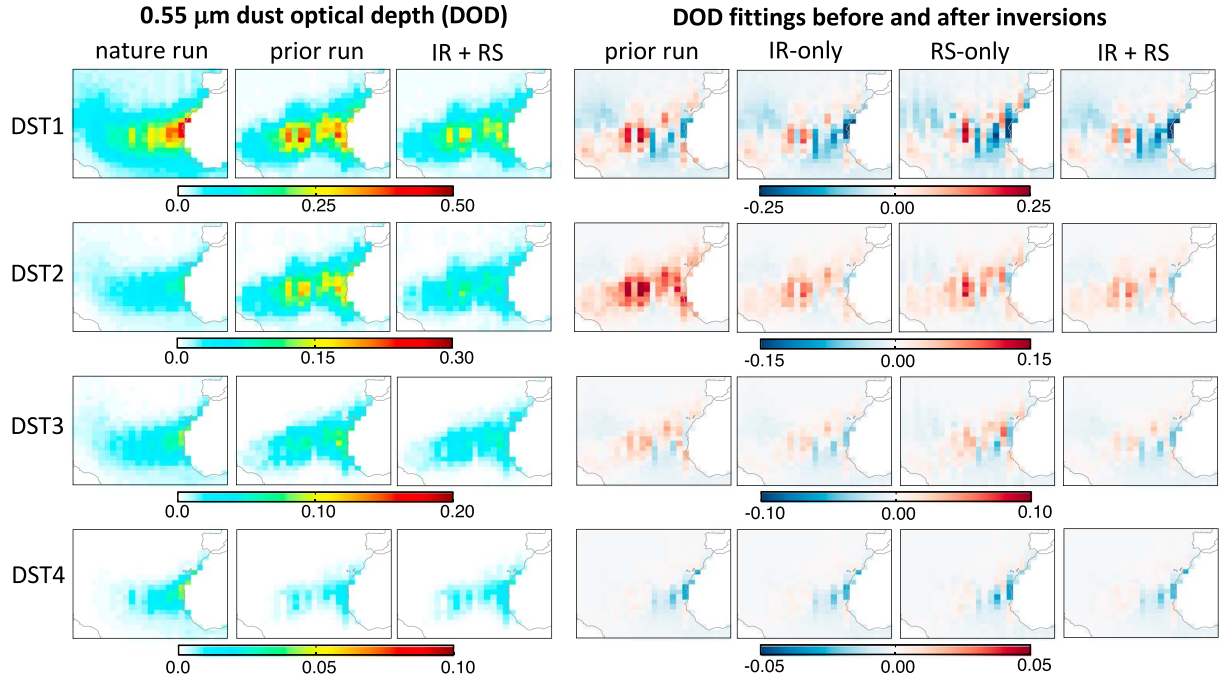

Figure 10. Fitting of synthetic DOD of each size bin before and after inversions. (first column) The distribution of synthetic CLARREO 0.55 μm DOD generated from the FIM-Chem nature run. (second and third columns) Prior and IR + RS constrained GEOS-Chem 0.55 μm DOD corresponding to synthetic CLARREO data, respectively. (fourth to seventh columns) The difference in DOD between synthetic data and prior GEOS-Chem simulations, and posterior GEOS-Chem simulations for inversions based IR only, RS only, and IR + RS inversions. In the DOD difference plots, red indicates that GEOS-Chem DOD is higher than synthetic CLARREO DOD.

3.3. OSSEs for Recovering Dust Emissions

The synthetic CLARREO DODs and their uncertainties characterized by the synthetic spectra are assimilated into the GEOS-Chem adjoint model in our OSSEs. Dust emissions of each size bin over Saharan deserts are iteratively constrained using the 4D-Var technique. The cost function (equation (6)) is reduced by about 50% after five iterations, and subsequent iterations yield negligible further reductions. We then choose the emissions constrained in the seventh iteration as our posterior solution.

Figure 10 presents the fittings of synthetic CLARREO DODs of each size bin before and after inversion of dust emissions. In the nature run, dust aerosols travel over Atlantic Ocean from Northern Africa to areas between Northern America and Central America. In contrast, the dust aerosols simulated by the prior GEOS-Chem run are transported to the lower latitude central America. Compared to the nature run, prior GEOS-Chem simulation overestimates the DOD of DST2 and DST3 and underestimates the DOD of DST4 over the downwind Atlantic Ocean. The DOD of DST1 of GEOS-Chem has a negative bias over the downwind flow near the coastal region but has positive bias over central to western Atlantic Ocean. These discrepancies between FIM-Chem and GEOS-Chem at any given time and location might be attributed to differences of emission, transport, and dry and wet deposition processes in these two models. However, our inversion assumes that such discrepancies integrated over time and space only reflect the difference in emission estimates, and our OSSEs solely adjust dust emission to fit the GEOS-Chem simulation to the synthetic data. This assumption represents a limitation of the inversion applied to emissions. Alleviating this limitation requires improved parametrizations of transport and deposition, inclusion of transport and deposition parameters in the control vector of the inversion, or formally addressing uncertainties in these processes within the inversion with weak-constraint 4D-Var techniques. However, the use of FIM-Chem to generate synthetic data and GEOS-Chem for data assimilation, which avoids the "identical-twin" OSSEs, at least allows us to evaluate how the differences between the models may be reflected in the posterior emission totals and distributions.

With the assimilation of synthetic data, posterior DODs are overall more consistent with the nature run, with improvements most apparent for DST2 and DST3 (Figure 10, second and third rows). Overestimation of DST2 and DST3 in the prior GEOS-Chem simulation is reduced for all observation scenarios and particularly

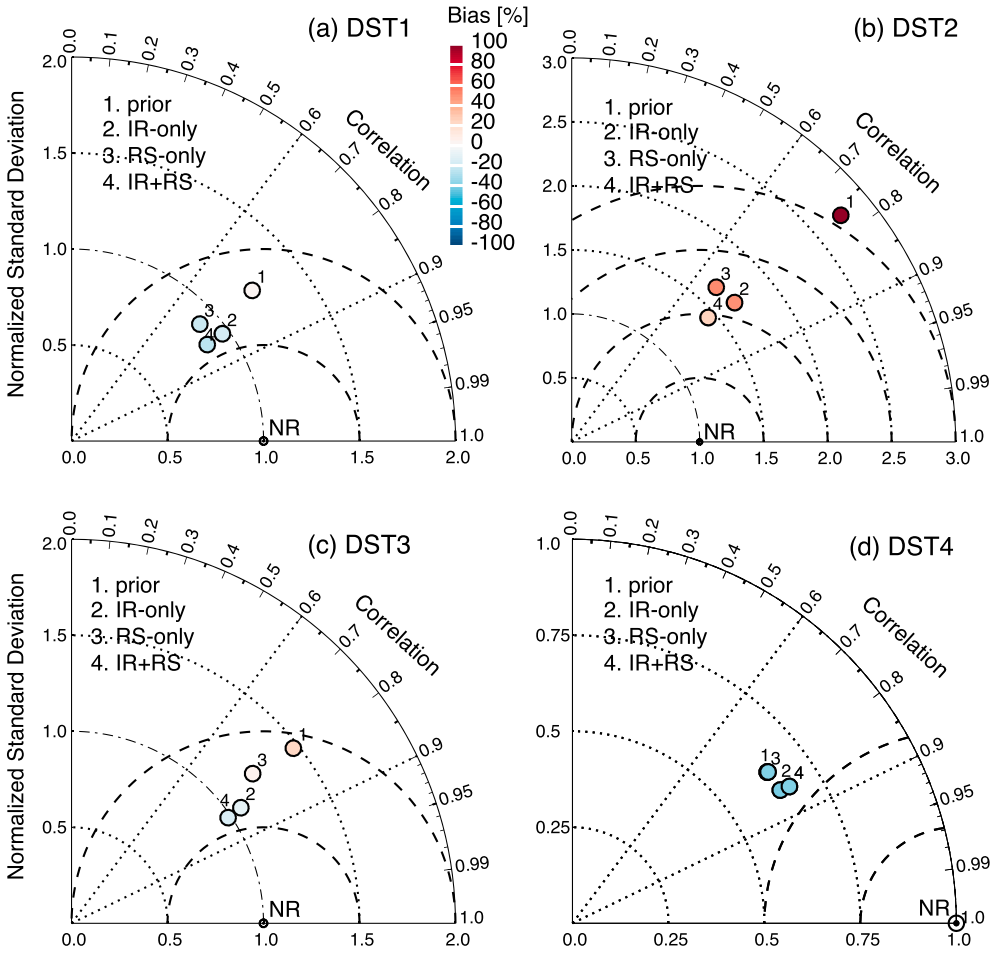

Figure 11. Taylor diagrams for comparison of GEOS-Chem DOD to nature run (NR) before and after inversions of different scenarios of synthetic CLARREO data. (a–d) DOD per bin from DST1 to DST4. Pearson correlation coefficient is indicated by the cosine of polar angle, the ratio of standard deviations (normalized standard deviation) by the radius axis, and the root-mean-square difference by the distance of the scatters to the "NR" point. In each panel, circles are labeled with a number to indicate the data pairs between prior, IR only, RS only, and IR + RS constrained GEOS-Chem DOD and NR DODs. The color of circle is coded with normalized mean bias.

when including IR measurements. In contrast, negligible improvement is found in posterior GEOS-Chem simulations of DST1 and DST4. While overestimation of DST1 over the central Atlantic Ocean is reduced, its underestimation over the African coastal ocean is enhanced. In this case, the different distributions of DST1 between the two models may be influenced by systematic differences in model processes other than emission, for instance, the wet deposition and transport. Distributions of DST4 show negligible change after data assimilation possibly owing to the weakest sensitivity of the measurements to dust in the largest size bin. In addition, there are north-south stripes evident in the difference plots, which is caused by the observation sampling: sampled DODs in the adjacent stripes are from simulations on different days owing to CLARREO's narrow swath (Figure 3).

Taylor diagrams (name after *Taylor* [2001]) are presented in Figure 11 to evaluate the consistency of DOD between GEOS-Chem and nature run (NR) before and after the inversions of different scenarios of synthetic CLARREO data. Each panel indicates DOD per bin from DST1 to DST4, respectively. Taylor diagram can effectively summarize multiple aspects of model performance including Pearson correlation coefficient in the polar axis, the ratio of standard deviations (normalized standard deviation) in the radius axis, and the root-mean-square difference (RMSD, the distance of the scatters to the point "NR"). In each panel, circles are labeled with a number to indicate the evaluation of prior, IR only, RS only, and IR + RS constrained

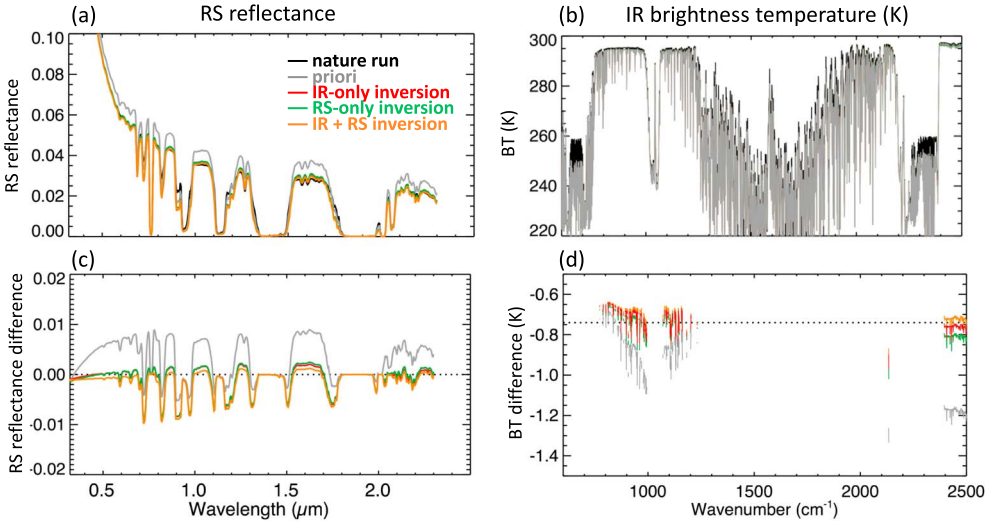

Figure 12. Spectral fitting of (a and c) RS reflectance and (b and d) IR BT before and after the inversions. (a and b) The reflectance and BT spectra. (c and d) The difference of spectra between the CLARREO synthetic data and GEOS-Chem simulation. Figure 12d only displays the spectra with transmittance larger than 85%.

GEOS-Chem DOD against the nature run. Overall, while the posterior DOD from those three observation scenarios are more consistent with "NR" with reduced RMSD and lower bias, the combined IR and RS can yield a slightly better agreement.

As discussed in section 2.6, the assimilation of DOD in our OSSEs is designed to be equivalent to direct assimilation of radiance spectra. Thus, we expect that the posterior GEOS-Chem simulation can better reproduce synthetic CLARREO spectra. The spectral shape of RS reflectance and IR radiance is affected not only by aerosol scattering and absorption but also the absorption of trace gases and the thermal state of the atmosphere and surface. Water vapor is the trace gas that absorbs and emits radiation across a considerably wide spectral range in NIR and IR. As a result, the differences of spectra between GEOS-Chem and FIM-Chem nature run are attributed to differences in abundance of trace gases and temperature of air and surface in addition to the discrepancy of aerosol loading. Therefore, we assess the spectral fitting only over atmospheric window regions, where the impact from trace gases is minimal. As shown in Figure 12, assimilation of DODs

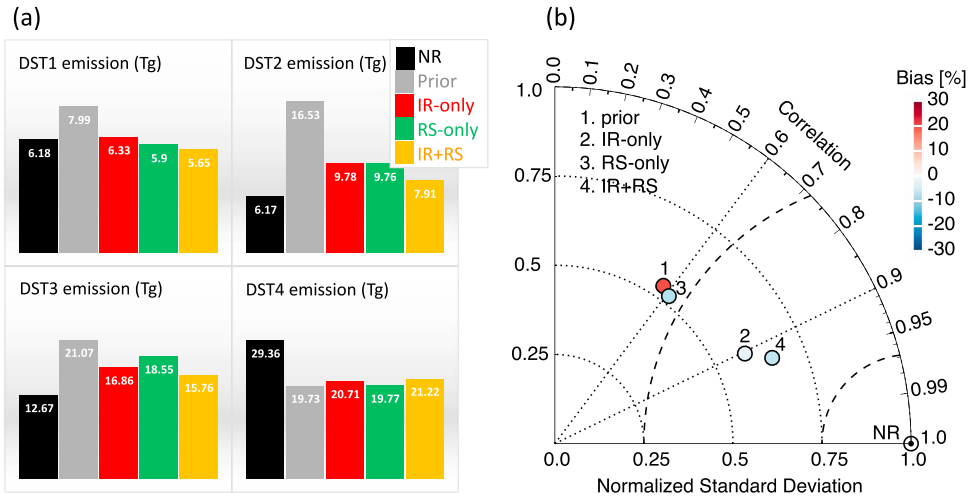

Figure 13. Comparisons of the dust emissions of each size bin between GEOS-Chem and nature run before and after assimilation of CLARREO synthetic data. (a) The total emitting amounts for each size bin. (b) Taylor diagram to illustrate the statics of total emission of each size bin shown in Figure 13a.

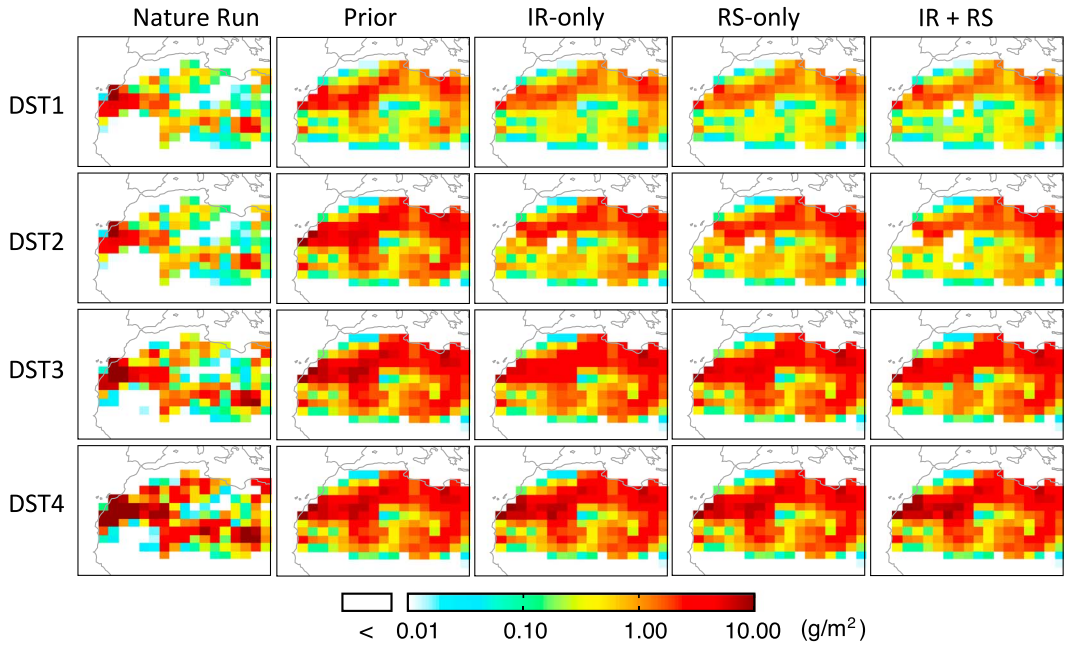

Figure 14. Comparisons of GEOS-Chem mineral dust emissions of each size bin before and after assimilating CLARREO data with nature-run dust emissions. (first column) Month dust emission fluxes simulated in FIM-Chem nature run and (second column) GEOS-Chem prior run. (third to fifth columns) The constrained dust emission fluxes with three scenarios of synthetic CLARREO data, i.e., IR only, RS only, and combined IR and RS, respectively.

significantly reduces the disagreements between GEOS-Chem and synthetic spectra in the atmospheric windows in shortwave spectral regions. In the IR atmospheric windows, the BT differences between GEOS-Chem and the synthetic data approach to 0.6–0.8 K, around the average difference of sea surface temperature between GEOS-Chem and FIM-Chem.

Figure 13 compares prior and posterior GEOS-Chem dust emissions to those modeled in the FIM-Chem nature run (or the "truth") for each size bin. Compared to the nature run, the prior GEOS-Chem simulation underestimates emission of DST4 by 33% but overestimates emissions of DST1, DST2, and DST3 by 29%, 168%, and 66%, respectively. The total amount of prior dust emissions is about 30% larger than that of the nature run. Assimilation of CLARREO synthetic data reduces the emission differences between GEOS-Chem and FIM-Chem for all four size bins, bringing the overall emission difference down to less than 8%. Improvements are most apparent for emissions of DST1 and DST2 for all measurement configurations and for DST3 for measurements including IR spectra. The mass partitioning of dust emissions among those four size bins is in better agreement after inversions. The correlation coefficient of dust emissions of each bin between GEOS-Chem and FIM-Chem increases from 0.59 prior to inversion to 0.62, 0.90, and 0.92 posterior to the RS only, IR only, and IR + RS inversions, respectively. Therefore, combined RS and IR spectra yield the greatest improvements in the constrained size-resolved dust emissions. Also, IR measurements, compared with RS measurements, provide most of the overall improvement. This is because adjustments of dust emissions are more significant over larger sizes, for which the IR spectra hold more information (Figure 8).

From CLARREO measurements, our long-term aim is to identify the trend of dust emission and loading on regional to global scales. Due to its narrow swath, CLARREO data may not have the capability to constrain the spatial distribution of dust sources at the model-level resolution. CLARREO RS and IR spectrometers only scan the near-nadir region, and the daily data samplings are sparse [*Wielicki et al*., 2013]. The time used by the satellite to establish a sufficient spatial coverage is much longer than that needed to capture the evolution of dust episodes. Therefore, assimilation of CLARREO data will unlikely improve the spatial distribution of episodic dust emissions. Figure 14 shows the spatial distributions of dust emissions for each size bin from the nature run and GEOS-Chem simulations before and after inversions. The change in the spatial pattern of the dust emissions after data assimilation is insignificant compared with the change of the total amount of regional

dust productions presented in Figure 13. Observations of larger spatial coverages will likely have more constraints on the spatial variability of dust emissions. As demonstrated by many previous studies, satellite sensors of wide swath (e.g., Moderate Resolution Imaging Spectroradiometer) can be applied to constrain spatial distribution of dust emission estimates [e.g., *Wang et al*., 2012; *Xu et al*., 2013; *Yumimoto and Takemura*, 2015]. Furthermore, CLARREO will intercalibrate other operational satellite sensors (e.g., Visible Infrared Imaging Radiometer Suite, VIIRS) and make them more accurate. Ultimately, spatial coverage can be significantly improved from joint CLARREO and other sensors with wide swath.

4. Discussion and Conclusions

The CLARREO satellite has been proposed to use spectrometers to measure the spectra of reflected solar (RS) radiation in UV-visible-NIR spectrum and infrared radiances (IR) measured from space. Its observation accuracy will be about 5–10 times better than any current operational satellite measurements. This study aims to identify the spectral fingerprint of mineral dust from CLARREO-like observation data and to evaluate the information content of these measurements for recovering size-resolved dust loading and for constraining dust emissions. Toward this goal, we have conducted a suite of observation system simulation experiments (OSSEs) for trans-Atlantic dust aerosols during June 2011. The OSSEs first generate synthetic CLARREO spectra of reflected solar radiation (RS) and Earth-emitted infrared radiance (IR), which are calculated by the UNL-VRTM radiative transfer model based on a FIM-Chem nature run. The spectral signals are then used for analyzing the sensitivities and error characteristics of dust optical depth (DOD) for three observations scenarios (IR only, RS only, and combined IR and RS) using an optimal estimation technique. Next, these synthetic data of different observation scenarios are assimilated into the GEOS-Chem adjoint model to constrain dust emissions of four size bins (with radii from 0.1 μm to 6.0 μm) using an adjoint-based four-dimensional variational technique.

The findings from information content analysis and OSSEs can be summarized as the following. (1) The IR spectra are most sensitive to dust loading and emissions of the third (1.8–3.0 μm radii) or larger size bin and least sensitive to the smallest size bin (0.1–1.0 μm radii). (2) In contrast, the RS spectra are most sensitive to dust of the smallest size bin, and sensitivity decreases as dust size increases. (3) Combining IR and RS spectra can fully characterize dust size, providing the best constraints for size-resolved dust emissions on a regional scale. (4) However, CLARREO data fail to constrain the spatial distribution of emitting sources in a model level resolution possibly due to its narrow nadir scan.

Observations of larger spatial coverages or over a longer time period will likely have more constraints on the spatial variability of dust emissions. The CLARREO Pathfinder Mission (CPF) will deploy a RS spectrometer on the International Space Station in the 2020 time frame [*Wielicki et al*., 2016]. One of the science objectives of the CPF mission is to demonstrate the multiinstrument intercalibration framework. Considering that the full CLARREO mission will intercalibrate other operational satellite sensors for both IR and RS measurements and make them more accurate, their joint spatial coverage with intercalibrated sensors will substantially increase. Therefore, we expect these joint measurements will provide improved spatial constraints for size-resolved dust emission and loading.

Finally, we should note that this study focuses on OSSEs of trans-Atlantic dust aerosols emitted from the Saharan desert in order to minimize the influence by aerosols from other sources. Application of the OSSE to other continents, such as Asia, will require the consideration of other aerosol species and will be studied in the near future.

Acknowledgments
This research is supported by the National Aeronautics and Space Administration under grant NNX17AF78G issued through the Atmospheric Composition Spectral Climate Signal Program managed by Hal Maring and NNX17AF77G issued through ACMAP program managed by Richard Eckman. We acknowledge the computational support from the Holland Computing Center at the University of Nebraska and the High Performance Computing group at The University of Iowa. All the data presented in this manuscript will be made available through Coalition on Publishing Data in the Earth and Space Sciences (https://copdessdirectory.osf.io) and please email J. Wang (jun-wang-1@uiowa.edu) and X. Xu (xiaoguang-xu@uiowa.edu) for details.

References

Ackerman, S. A. (1997), Remote sensing aerosols using satellite infrared observations, *J. Geophys. Res.*, *102*, 17,069–17,079, doi:10.1029/96JD03066.

Alexander, B., R. J. Park, D. J. Jacob, Q. B. Li, R. M. Yantosca, J. Savarino, C. C. W. Lee, and M. H. Thiemens (2005), Sulfate formation in sea-salt aerosols: Constraints from oxygen isotopes, *J. Geophys. Res.*, *110*, D10307, doi:10.1029/2004JD005659.

Arnold, C. P., and C. H. Dey (1986), Observing-systems simulation experiments: Past, present, and future, *Bull. Am. Meteorol. Soc.*, *67*(6), 687–695.

Baldridge, A. M., S. J. Hook, C. I. Grove, and G. Rivera (2009), The ASTER spectral library version 2.0, *Remote Sens. Environ.*, *113*(4), 711–715.

Bey, I., D. J. Jacob, R. M. Yantosca, J. A. Logan, B. D. Field, A. M. Fiore, Q. Li, H. Y. Liu, L. J. Mickley, and M. G. Schultz (2001), Global modeling of tropospheric chemistry with assimilated meteorology: Model description and evaluation, *J. Geophys. Res.*, *106*, 23,073–23,095, doi:10.1029/2001JD000807.

Bleck, R., et al. (2015), A vertically flow-following icosahedral grid model for medium-range and seasonal prediction. Part I: Model description, *Mon. Weather Rev.*, *143*, 2386–2403.

Boucher, O., et al. (2013), Clouds and aerosols, in *Climate Change 2013: The Physical Science Basis. Contribution of Working Group I to the Fifth Assessment Report of the Intergovernmental Panel on Climate Change*, edited by T. F. Stocker et al., pp. 571–657, Cambridge Univ. Press, Cambridge, U. K., and New York.

Bovensmann, H., J. P. Burrows, M. Buchwitz, J. Frerick, S. Noël, V. V. Rozanov, K. V. Chance, and A. P. H. Goede (1999), SCIAMACHY: Mission objectives and measurement modes, *J. Atmos. Sci.*, *56*(2), 127–150.

Burrows, J. P., et al. (1999), The Global Ozone Monitoring Experiment (GOME): Mission concept and first scientific results, *J. Atmos. Sci.*, *56*(2), 151–175.

Byrd, R. H., J. Nocedal, and R. B. Schnabel (1994), Representations of quasi-Newton matrices and their use in limited memory methods, *Math. Program.*, *63*(2), 129–156.

Chahine, M. T., et al. (2006), AIRS: Improving weather forecasting and providing new data on greenhouse gases, *Bull. Am. Meteorol. Soc.*, *87*(7), 911–926.

Chin, M., R. B. Rood, S.-J. Lin, J.-F. Müller, and A. M. Thompson (2000), Atmospheric sulfur cycle simulated in the global model GOCART: Model description and global properties, *J. Geophys. Res.*, *105*, 24,671–24,687, doi:10.1029/2000JD900384.

Chin, M., P. Ginoux, S. Kinne, O. Torres, B. N. Holben, B. N. Duncan, R. V. Martin, J. A. Logan, A. Higurashi, and T. Nakajima (2002), Tropospheric aerosol optical thickness from the GOCART model and comparisons with satellite and Sun photometer measurements, *J. Atmos. Sci.*, *59*(3), 461–483.

Di Biagio, C., H. Boucher, S. Caquineau, S. Chevaillier, J. Cuesta, and P. Formenti (2014), Variability of the infrared complex refractive index of African mineral dust: Experimental estimation and implications for radiative transfer and satellite remote sensing, *Atmos. Chem. Phys.*, *14*(20), 11,093–11,116.

Di Biagio, C., et al. (2017), Global scale variability of the mineral dust long-wave refractive index: A new dataset of in situ measurements for climate modeling and remote sensing, *Atmos. Chem. Phys.*, *17*(3), 1901–1929.

Ding, S., J. Wang, and X. Xu (2016), Polarimetric remote sensing in oxygen A and B bands: Sensitivity study and information content analysis for vertical profile of aerosols, *Atmos. Meas. Tech.*, *9*(5), 2077–2092.

Drury, E., D. J. Jacob, R. J. D. Spurr, J. Wang, Y. Shinozuka, B. E. Anderson, A. D. Clarke, J. Dibb, C. McNaughton, and R. Weber (2010), Synthesis of satellite (MODIS), aircraft (ICARTT), and surface (IMPROVE, EPA-AQS, AERONET) aerosol observations over eastern North America to improve MODIS aerosol retrievals and constrain surface aerosol concentrations and sources, *J. Geophys. Res.*, *115*, D14204, doi:10.1029/2009JD012629.

Edwards, D. P., A. F. Arellano, and M. N. Deeter (2009), A satellite observation system simulation experiment for carbon monoxide in the lowermost troposphere, *J. Geophys. Res.*, *114*, D14304, doi:10.1029/2008JD011375.

Emery, W. J., D. J. Baldwin, P. Schlüssel, and R. W. Reynolds (2001), Accuracy of in situ sea surface temperatures used to calibrate infrared satellite measurements, *J. Geophys. Res.*, *106*, 2387–2405, doi:10.1029/2000JC000246.

Evans, M. J., and D. J. Jacob (2005), Impact of new laboratory studies of N_2O_5 hydrolysis on global model budgets of tropospheric nitrogen oxides, ozone, and OH, *Geophys. Res. Lett.*, *32*, L09813, doi:10.1029/2005GL022469.

Fairlie, D. T., D. J. Jacob, and R. J. Park (2007), The impact of transpacific transport of mineral dust in the United States, *Atmos. Environ.*, *41*(6), 1251–1266.

Feldman, D. R., C. A. Algieri, J. R. Ong, and W. D. Collins (2011), CLARREO shortwave observing system simulation experiments of the twenty-first century: Simulator design and implementation, *J. Geophys. Res.*, *116*, D10107, doi:10.1029/2010JD015350.

Feldman, D. R., W. D. Collins, and J. L. Paige (2015), Pan-spectral observing system simulation experiments of shortwave reflectance and long-wave radiance for climate model evaluation, *Geosci. Model Dev.*, *8*(7), 1943–1954.

Fox, N., et al. (2003), Traceable radiometry underpinning terrestrial- and helio-studies (TRUTHS), *Adv. Space Res.*, *32*(11), 2253–2261.

Fox, N., A. Kaiser-Weiss, W. Schmutz, K. Thome, D. Young, B. Wielicki, R. Winkler, and E. Woolliams (2011), Accurate radiometry from space: An essential tool for climate studies, *Phil. Trans. R. Soc. A*, *369*(1953), 4028–4063.

Frigge, M., D. C. Hoaglin, and B. Iglewicz (1989), Some implementations of the boxplot, *Am. Stat.*, *43*(1), 50–54.

Gillette, D. (1978), A wind tunnel simulation of the erosion of soil: Effect of soil texture, sandblasting, wind speed, and soil consolidation on dust production, *Atmos. Environ.*, *12*(8), 1735–1743.

Ginoux, P., M. Chin, I. Tegen, J. M. Prospero, B. Holben, O. Dubovik, and S.-J. Lin (2001), Sources and distributions of dust aerosols simulated with the GOCART model, *J. Geophys. Res.*, *106*, 20,255–20,273, doi:10.1029/2000JD000053.

Grell, G. A., S. A. McKeen, S. R. Freitas, S. Sahm, and S. Sun (2013), Updates to ESRL's FIM-Chem global modeling system and comparison of aerosol optical depth forecasts with AERONET observations, 2013 NOAA ESRL Global Monitoring Annual Conference, Boulder, Colo.

Guan, X., J. Huang, Y. Zhang, Y. Xie, and J. Liu (2016), The relationship between anthropogenic dust and population over global semi-arid regions, *Atmos. Chem. Phys.*, *16*(8), 5159–5169.

Hagan, D. E., and P. J. Minnett (2003), AIRS radiance validation over ocean from sea surface temperature measurements, *IEEE Trans. Geosci. Remote Sens.*, *41*(2), 432–441.

Han, Y., et al. (2013), Suomi NPP CrIS measurements, sensor data record algorithm, calibration and validation activities, and record data quality, *J. Geophys. Res. Atmos.*, *118*, 12,734–712,748, doi:10.1002/2013JD020344.

Henze, D. K., A. Hakami, and J. H. Seinfeld (2007), Development of the adjoint of GEOS-Chem, *Atmos. Chem. Phys.*, *7*(9), 2413–2433.

Henze, D. K., J. H. Seinfeld, and D. T. Shindell (2009), Inverse modeling and mapping US air quality influences of inorganic $PM_{2.5}$ precursor emissions using the adjoint of GEOS-Chem, *Atmos. Chem. Phys.*, *9*(16), 5877–5903.

Hilton, F., et al. (2012), Hyperspectral Earth observation from IASI: Five years of accomplishments, *Bull. Am. Meteorol. Soc.*, *93*(3), 347–370.

Hou, W., J. Wang, X. Xu, J. S. Reid, and D. Han (2016), An algorithm for hyperspectral remote sensing of aerosols: 1. Development of theoretical framework, *J. Quant. Spectrosc. Radiat. Transfer*, *178*, 400–415.

Hou, W., J. Wang, X. Xu, and J. S. Reid (2017), An algorithm for hyperspectral remote sensing of aerosols: 2. Information content analysis for aerosol parameters and principal components of surface spectra, *J. Quant. Spectrosc. Radiat. Transfer*, *192*, 14–29.

Huneeus, N., et al. (2011), Global dust model intercomparison in AeroCom phase I, *Atmos. Chem. Phys.*, *11*(15), 7781–7816.

Iversen, J. D., and B. R. White (1982), Saltation threshold on Earth, Mars and Venus, *Sedimentology*, *29*(1), 111–119.

Jacob, D. J. (2000), Heterogeneous chemistry and tropospheric ozone, *Atmos. Environ.*, *34*(12–14), 2131–2159.

Jaeglé, L., P. K. Quinn, T. S. Bates, B. Alexander, and J. T. Lin (2011), Global distribution of sea salt aerosols: New constraints from in situ and remote sensing observations, *Atmos. Chem. Phys.*, *11*(7), 3137–3157.

Jin, Z., and M. Sun (2016), An Initial Study on Climate Change Fingerprinting Using the Reflected Solar Spectra, *J. Clim.*, *29*(8), 2781–2796, doi:10.1175/jcli-d-15-0297.1.

Johnson, M. S., N. Meskhidze, and V. Praju Kiliyanpilakkil (2012), A global comparison of GEOS-Chem-predicted and remotely-sensed mineral dust aerosol optical depth and extinction profiles, *J. Adv. Model. Earth Syst.*, *4*(3), M07001.

Jones, S. L., R. Adams-Selin, E. D. Hunt, G. A. Creighton, and J. D. Cetola (2012), Update on modifications to WRF-CHEM GOCART for fine-scale dust forecasting at AFWA, Abstarct A33D-0188 presented at 2012 Fall Meeting, AGU, San Francisco, Calif., 3–7 Dec.

Kawamura, R. (1951), Study of sand movement by wind, Reports of Physical Sciences Research Institute of Tokyo University [in Japanese], vol. 5, pp. 95–112, NASA, Washington, D. C.

Klüser, L., J. R. Banks, D. Martynenko, C. Bergemann, H. E. Brindley, and T. Holzer-Popp (2015), Information content of space-borne hyperspectral infrared observations with respect to mineral dust properties, *Remote Sens. Environ.*, *156*, 294–309.

Knippertz, P., and M. C. Todd (2012), Mineral dust aerosols over the Sahara: Meteorological controls on emission and transport and implications for modeling, *Rev. Geophys.*, *50*, RG1007, doi:10.1029/2011RG000362.

Kok, J. F. (2011), A scaling theory for the size distribution of emitted dust aerosols suggests climate models underestimate the size of the global dust cycle, *Proc. Natl. Acad. Sci. U.S.A.*, *108*(3), 1016–1021.

Kok, J. F., D. A. Ridley, Q. Zhou, R. L. Miller, C. Zhao, C. L. Heald, D. S. Ward, S. Albani, and K. Haustein (2017), Smaller desert dust cooling effect estimated from analysis of dust size and abundance, *Nat. Geosci.*, *10*(4), 274–278.

Lee, C. M., M. L. Cable, S. J. Hook, R. O. Green, S. L. Ustin, D. J. Mandl, and E. M. Middleton (2015), An introduction to the NASA Hyperspectral InfraRed imager (HyspIRI) mission and preparatory activities, *Remote Sens. Environ.*, *167*, 6–19.

Luo, C., N. Mahowald, and C. Jones (2004), Temporal variability of dust mobilization and concentration in source regions, *J. Geophys. Res.*, *109*, D20202, doi:10.1029/2004JD004861.

Mahowald, N., C. Luo, J. del Corral, and C. S. Zender (2003), Interannual variability in atmospheric mineral aerosols from a 22-year model simulation and observational data, *J. Geophys. Res.*, *108*(D12), 4352, doi:10.1029/2002JD002821.

Mahowald, N., S. Albani, J. F. Kok, S. Engelstaeder, R. Scanza, D. S. Ward, and M. G. Flanner (2014), The size distribution of desert dust aerosols and its impact on the earth system, *Aeolian Res.*, *15*, 53–71.

Maring, H., D. L. Savoie, M. A. Izaguirre, L. Custals, and J. S. Reid (2003), Mineral dust aerosol size distribution change during atmospheric transport, *J. Geophys. Res.*, *108*(D19), 8592, doi:10.1029/2002JD002536.

Marticorena, B., and G. Bergametti (1995), Modeling the atmospheric dust cycle: 1. Design of a soil-derived dust emission scheme, *J. Geophys. Res.*, *100*, 16,415–16,430, doi:10.1029/95JD00690.

Martin, R. V., D. J. Jacob, R. M. Yantosca, M. Chin, and P. Ginoux (2003), Global and regional decreases in tropospheric oxidants from photochemical effects of aerosols, *J. Geophys. Res.*, *108*(D3), 4097, doi:10.1029/2002JD002622.

Masutani, M., T. W. Schlatter, R. M. Errico, A. Stoffelen, E. Andersson, W. Lahoz, J. S. Woollen, G. D. Emmitt, L.-P. Riishøjgaard, and S. J. Lord (2010), Observing system simulation experiments, in *Data Assimilation: Making Sense of Observations*, edited by W. Lahoz, B. Khattatov, and R. Menard, pp. 647–679, Springer, Berlin, Heidelberg.

McClatchey, R. A., R. W. Fenn, J. E. A. Selby, F. E. Volz, and J. S. Garing (1972), Optical properties of atmosphere, 3rd ed., AFCRL-72-0497.

Meland, B. S., X. Xu, D. K. Henze, and J. Wang (2013), Assessing remote polarimetric measurement sensitivities to aerosol emissions using the GEOS-Chem adjoint model, *Atmos. Meas. Tech.*, *6*(12), 3441–3457.

Munro, R., et al. (2016), The GOME-2 instrument on the Metop series of satellites: Instrument design, calibration, and level 1 data processing—An overview, *Atmos. Meas. Tech.*, *9*(3), 1279–1301.

Park, R. J., D. J. Jacob, M. Chin, and R. V. Martin (2003), Sources of carbonaceous aerosols over the United States and implications for natural visibility, *J. Geophys. Res.*, *108*(D12), 4355, doi:10.1029/2002JD003190.

Park, R. J., D. J. Jacob, B. D. Field, R. M. Yantosca, and M. Chin (2004), Natural and transboundary pollution influences on sulfate-nitrate-ammonium aerosols in the United States: Implications for policy, *J. Geophys. Res.*, *109*, D15204, doi:10.1029/2003JD004473.

Patterson, E. M., D. A. Gillette, and B. H. Stockton (1977), Complex index of refraction between 300 and 700 nm for Saharan aerosols, *J. Geophys. Res.*, *82*, 3153–3160, doi:10.1029/JC082i021p03153.

Perlwitz, J. P., C. Pérez García-Pando, and R. L. Miller (2015), Predicting the mineral composition of dust aerosols—Part 1: Representing key processes, *Atmos. Chem. Phys.*, *15*(20), 11,593–11,627.

Pierangelo, C., A. Chédin, S. Heilliette, N. Jacquinet-Husson, and R. Armante (2004), Dust altitude and infrared optical depth from AIRS, *Atmos. Chem. Phys.*, *4*(7), 1813–1822.

Pierangelo, C., M. I. Mishchenko, Y. Balkanski, and A. Chedin (2005), Retrieving the effective radius of Saharan dust coarse mode from AIRS, *Geophys. Res. Lett.*, *32*, L20813, doi:10.1029/2005GL023425.

Qu, Z., D. K. Henze, S. L. Capps, Y. Wang, X. Xu, and J. Wang (2016), Monthly top-down NOx emissions for China (2005–2012): A hybrid inversion method and trend analysis, *J. Geophys. Res. Atmos.*, *122*, 4600–4625, doi:10.1002/2016JD025852.

Reid, J. S., E. A. Reid, A. Walker, S. Piketh, S. Cliff, A. Al Mandoos, S.-C. Tsay, and T. F. Eck (2008), Dynamics of southwest Asian dust particle size characteristics with implications for global dust research, *J. Geophys. Res.*, *113*, D14212, doi:10.1029/2007JD009752.

Ridley, D. A., C. L. Heald, and J. M. Prospero (2014), What controls the recent changes in African mineral dust aerosol across the Atlantic?, *Atmos. Chem. Phys.*, *14*(11), 5735–5747.

Ridley, D. A., C. L. Heald, J. F. Kok, and C. Zhao (2016), An observationally constrained estimate of global dust aerosol optical depth, *Atmos. Chem. Phys.*, *16*(23), 15,097–15,117.

Rodgers, C. D. (2000), Inverse Methods for Atmospheric Sounding: Theory and Practice, 258 pp., World Scientific, Singapore.

Ryder, C. L., E. J. Highwood, T. M. Lai, H. Sodemann, and J. H. Marsham (2013), Impact of atmospheric transport on the evolution of microphysical and optical properties of Saharan dust, *Geophys. Res. Lett.*, *40*, 2433–2438, doi:10.1002/grl.50482.

Scanza, R. A., N. Mahowald, S. Ghan, C. S. Zender, J. F. Kok, X. Liu, Y. Zhang, and S. Albani (2015), Modeling dust as component minerals in the community atmosphere model: Development of framework and impact on radiative forcing, *Atmos. Chem. Phys.*, *15*(1), 537–561.

Sokolik, I. N. (2002), The spectral radiative signature of wind-blown mineral dust: Implications for remote sensing in the thermal IR region, *Geophys. Res. Lett.*, *29*(24), 2154, doi:10.1029/2002GL015910.

Spurr, R. (2006), VLIDORT: A linearized pseudo-spherical vector discrete ordinate radiative transfer code for forward model and retrieval studies in multilayer multiple scattering media, *J. Quant. Spectrosc. Radiat. Transfer*, *102*, 316–342.

Spurr, R., J. Wang, J. Zeng, and M. I. Mishchenko (2012), Linearized T-matrix and Mie scattering computations, *J. Quant. Spectrosc. Radiat. Transfer*, *113*(6), 425–439.

Spurr, R. J. D. (2004), A new approach to the retrieval of surface properties from earthshine measurements, *J. Quant. Spectrosc. Radiat. Transfer*, *83*(1), 15–46.

Su, L., and J. C. H. Fung (2015), Sensitivities of WRF-Chem to dust emission schemes and land surface properties in simulating dust cycles during springtime over East Asia, *J. Geophys. Res. Atmos.*, *120*, 11,215–11,230, doi:10.1002/2015JD023446.

Taylor, K. E. (2001), Summarizing multiple aspects of model performance in a single diagram, *J. Geophys. Res.*, *106*, 7183–7192, doi:10.1029/2000JD900719.

Tegen, I., and A. A. Lacis (1996), Modeling of particle size distribution and its influence on the radiative properties of mineral dust aerosol, *J. Geophys. Res.*, *101*, 19,237–19,244, doi:10.1029/95JD03610.

Timmermans, R. M. A., M. Schaap, P. Builtjes, H. Elbern, R. Siddans, S. Tjemkes, and R. Vautard (2009), An observing system simulation experiment (OSSE) for aerosol optical depth from satellites, *J. Atmos. Oceanic Technol.*, *26*(12), 2673–2682.

Timmermans, R. M. A., W. A. Lahoz, J. L. Attié, V. H. Peuch, R. L. Curier, D. P. Edwards, H. J. Eskes, and P. J. H. Builtjes (2015), Observing system simulation experiments for air quality, *Atmos. Environ.*, *115*, 199–213.

Vandenbussche, S., S. Kochenova, A. C. Vandaele, N. Kumps, and M. De Mazière (2013), Retrieval of desert dust aerosol vertical profiles from IASI measurements in the TIR atmospheric window, *Atmos. Meas. Tech.*, *6*(10), 2577–2591.

Wang, J., S. A. Christopher, J. S. Reid, H. Maring, D. Savoie, B. N. Holben, J. M. Livingston, P. B. Russell, and S.-K. Yang (2003), GOES 8 retrieval of dust aerosol optical thickness over the Atlantic Ocean during PRIDE, *J. Geophys. Res.*, *108*(D19), 8595, doi:10.1029/2002JD002494.

Wang, J., X. Xu, D. K. Henze, J. Zeng, Q. Ji, S.-C. Tsay, and J. Huang (2012), Top-down estimate of dust emissions through integration of MODIS and MISR aerosol retrievals with the GEOS-Chem adjoint model, *Geophys. Res. Lett.*, *39*, L08802, doi:10.1029/2012GL051136.

Wang, J., X. Xu, S. Ding, J. Zeng, R. Spurr, X. Liu, K. Chance, and M. Mishchenko (2014), A numerical testbed for remote sensing of aerosols, and its demonstration for evaluating retrieval synergy from a geostationary satellite constellation of GEO-CAPE and GOES-R, *J. Quant. Spectrosc. Radiat. Transfer*, *146*, 510–528.

Wang, J., C. Aegerter, X. Xu, and J. J. Szykman (2016), Potential application of VIIRS day/night band for monitoring nighttime surface PM2.5 air quality from space, *Atmos. Environ.*, *124*, 55–63.

Wang, Y., J. Wang, X. Xu, D. K. Henze, Y. Wang, and Z. Qu (2016), A new approach for monthly updates of anthropogenic sulfur dioxide emissions from space: Application to China and implications for air quality forecasts, *Geophys. Res. Lett.*, *43*, 9931–9938, doi:10.1002/2016GL070204.

Wielicki, B. A., et al. (2013), Achieving climate change absolute accuracy in orbit, *Bull. Am. Meteorol. Soc.*, *94*(10), 1519–1539.

Wielicki, B. A., et al. (2016), Pathfinder mission for Climate Absolute Radiance and Refractivity Observatory, CLARREO Pathfinder Mission Team Report (June 2016), Editor-in-Chief: Yolanda L. S. [Availabe at http://clarreo.larc.nasa.gov.]

Xu, X., and J. Wang (2015), Retrieval of aerosol microphysical properties from AERONET photopolarimetric measurements: 1. Information content analysis, *J. Geophys. Res. Atmos.*, *120*, 7059–7078, doi:10.1002/2015JD023108.

Xu, X., J. Wang, D. K. Henze, W. Qu, and M. Kopacz (2013), Constraints on aerosol sources using GEOS-Chem adjoint and MODIS radiances, and evaluation with multisensor (OMI, MISR) data, *J. Geophys. Res. Atmos.*, *118*, 6396–6413, doi:10.1002/jgrd.50515.

Xu, X., et al. (2015), Retrieval of aerosol microphysical properties from AERONET photopolarimetric measurements: 2. A new research algorithm and case demonstration, *J. Geophys. Res. Atmos.*, *120*, 7079–7098, doi:10.1002/2015JD023113.

Xu X., J. Wang, Y. Wang, J. Zeng, O. Torres, Y. Yang, A. Marshak, J. Reid, and S. Miller (2017), Passive remote sensing of altitude and optical depth of dust plumes using the oxygen A and B bands: First results from EPIC/DSCOVR at Lagrange-1 point, *Geophys. Res. Lett.*, *44*, doi:10.1002/2017GL073939.

Yu, H., M. Chin, D. M. Winker, A. H. Omar, Z. Liu, C. Kittaka, and T. Diehl (2010), Global view of aerosol vertical distributions from CALIPSO lidar measurements and GOCART simulations: Regional and seasonal variations, *J. Geophys. Res.*, *115*, D00H30, doi:10.1029/2009JD013364.

Yumimoto, K., and T. Takemura (2015), Long-term inverse modeling of Asian dust: Interannual variations of its emission, transport, deposition, and radiative forcing, *J. Geophys. Res. Atmos.*, *120*, 1582–1607, doi:10.1002/2014JD022390.

Zender, C. S., H. Bian, and D. Newman (2003), Mineral dust entrainment and deposition (DEAD) model: Description and 1990s dust climatology, *J. Geophys. Res.*, *108*(D14), 4416, doi:10.1029/2002JD002775.

Zhang, L., J. F. Kok, D. K. Henze, Q. Li, and C. Zhao (2013), Improving simulations of fine dust surface concentrations over the western United States by optimizing the particle size distribution, *Geophys. Res. Lett.*, *40*, 3270–3275, doi:10.1002/grl.50591.

Zhang, L., G. A. Grell, D. K. Henze, and S. A. McKeen (2016a), Sensitivity of dust emissions to aerosol feedback using FIM-Chem, 2016 IGAC Meeting, 29 Sep 2016, Breckenridge, Colo.

Zhang, L., G. A. Grell, S. A. McKeen, and R. Ahmadov (2016b), The impact of more complex aerosol and chemistry modules on the aerosol predictions within a global online modeling system FIM-Chem, Abstract A11B-0016 presented at 2016 Fall Meeting, AGU, San Francisco, Calif., 12 Dec.

Zhu, C., R. H. Byrd, P. Lu, and J. Nocedal (1994), *L-BFGS-B: A Limited Memory FORTRAN Code for Solving Bound Constrained Optimization Problems*, Northwestern Univ., Evanston, Ill.